Numerical modelling of Multiphysics couplings and strain localization

F. Collin[1], P. Kotronis[2], B. Pardoen[3]

[1]Department ArGEnCo, University of Liège, Belgium ;

[2]GeM (Institut de Recherche en Génie Civil et Mécanique), Ecole Centrale de Nantes, France ;

[3]Department of Civil Engineering, Laval University, Canada.

Rupture in geomaterials is often preceded by a localization of the deformations within thin bands. The strain localization is therefore an important process, which has been studied both experimentally and theoretically. This paper summarizes the main observations on localized phenomena and proposes numerical tools to characterize localization processes. To deal with interactions occurring between the different phases of porous media, a regularization technique based on the second gradient model has been extended to multiphysic couplings.

1   Introduction

Since the material behaviour and rupture are of importance regarding the design of geotechnical works for which the materials can be subjected to strong solicitations, failure has been widely investigated in geomechanics. Experimental observations on geomaterials clearly indicate the appearance of localised ruptures [Des84]. Theoretically, the concept of rupture surface is one of the oldest case of material localised failure and was already used in the design of works and structures few centuries ago [Cou73]. In some cases, a diffuse mode of failure can also be observed and it corresponds to homogeneous failure in laboratory tests [KGDL06]. Nowadays, it is commonly assumed that localised deformation and damage can appear in materials prior to the rupture in many situations. In rock material, a stress redistribution can engender damage that can firstly be diffused then localised. Once the damage threshold is reached, microcracks initiate, then grow, accumulate, and propagate within the material. If the microcracks coalesce, the distributed damage can further lead to strain

localisation and to the initiation of interconnected fractures by the onset of macroc-racks, which provokes a sudden material rupture [Die03].

The fracturing process instigates discontinuities in the material that can be represented theoretically and numerically by various approaches. Two mains categories exist: the continuous and discrete descriptions of fracture. The continuous description includes material damage and strain localisation, while the discrete description explicitly repre-sents cracks. In fracture mechanics, the different fractures can be in tensile or opening mode (mode I), in sliding shear mode (mode II), in tearing shear mode (mode III), or in mixed-mode (mode I-II, [JS88]). The modelling of shear strain localisation is a con-tinuous approach that does not explicitly reproduce fractures and their discontinuities. Nevertheless, it generally induces the appearance of shear bands and a non-uniform strain distribution that may engender a displacement discontinuity between the mate-rial located on the two sides of a shear band.

Furthermore, soils and rocks are porous materials, where the porous volume is filled with one or several fluids (water, gas, oil ...). The general behaviour of the medium depends not only on the skeleton response (solid phase) to a given loading path, but also on the interactions occurring between the different phases of the medium. Cap-illary effects, temperature variations, chemical reactions induce specific behaviours, which have to be modelled by multiphysical constitutive laws. The numerical tools for modelling strain localization problems have thus to be extended to this multiphysic context, to deal with applications related, for instance, to nuclear waste disposal and concrete behaviour under severe loading. Then, new questions arise concerning the interactions between localization process and physical process (like liquid diffusion for example). The answer to these new questions can only be given by experimen-tal evidences. The section 2 of this paper summarizes the main observations on the localization phenomenon, coming from experimental results. Section 3 describes the regularization methods used to model properly the strain localization process. Section 4 is the description of the coupled second gradient model in saturated conditions. A biaxial compression test is modelled in order to show the ability of the second gradient model to represent correctly the post-peak behaviour. In section 5, the second gradient model is extended to unsaturated conditions . The example of a gallery excavation is proposed in section 6 to evidence the influence of hydro-mechanical couplings in satu-rated and unsaturated conditions on the strain localization process. Some conclusions end up the paper in section 7.

2   Experimental evidences of strain localisation

Strain localisation is frequently observed prior to material rupture. Starting from a homogeneous deformation state, strain localisation consists in a brutal accumulation of strain in a limited zone that can lead to cracks and failure (rupture lines). In geo-materials like soils and rocks it is often considered as a shear strain accumulation in band mode [Des05]. Nevertheless, the type of localisation may be of different nature

for other materials.

Geomaterials have low tensile strength, thus tensile rupture is arduous to characterise. On the other hand, plenty of small-scale compression laboratory tests are dedicated to strain localisation [VGG78, HD93, FHMV96, FHMV97, ABS03] and allow to characterise the compression material behaviour up to the rupture. They are generally realised on axisymmetric triaxial or plane-strain biaxial compression apparatus and involve special techniques, such as stereophotogrammetry [Des84, DV04], X-ray microtomography, and three dimensional digital image correlation [LBD$^+$07], to study the evolution of the strain localisation process. The advantage of biaxial compression experiments is that the localisation process is clearly evidenced, whereas it can remain hidden inside the sample in triaxial compression tests.

Under compressive regime, rupture is governed essentially by shear failure and these experimental studies generally highlight shear strain localisation in band mode [Des05]. It is commonly accepted that the shear band establishment corresponds to a peak stress in the stress-strain global response curve of the specimen [MD99, Des05].

The experimental localisation studies mostly analyse the behaviour of sand and only a few are actually available on rocks [BDR00]. Analysing the formation of fractures and strain localisation bands in rocks is quite challenging due to their high resistance and brittle behaviour (quasi-brittle material), thence the development of appropriate apparatus designed to test this type of material is necessary [DV04].

3   Regularisation methods

The further step is to define an appropriate and robust method that allows to properly model strain localisation and shear banding with the finite element method, leading finally to rupture in localised mode. Local descriptions of failure with classical finite element methods are not efficient in the reproduction of strain localisation because they suffer a mesh dependency (to mesh size and orientation) as indicated by [PM81], [ZPV01b], [CLC09], and [WW10]. This pathological problem is due to the properties of the underlying mathematical problem.

The dependence to the finite element discretisation can be solved by employing a proper regularisation technique. Such method has to introduce an internal length scale in the problem to model correctly the post-localisation behaviour. Two principal categories of enhanced models exist: one consists in the enrichment of the constitutive law with for instance non-local [BBC84, PCB87, PdBB$^+$96, GSH12] or gradient plasticity [Aif84, dBM92, PdBBdV96], the other approaches in the enrichment of the continuum kinematics with microstructure effects. For this second category the microkinematics are characterised at microscale in addition to the classical macrokinematics [CC09, Tou62, Min64, Ger73]. However, enhanced models restore mesh objectivity but not the uniqueness of the solution.

3.1   Enrichment of the constitutive law

In this approach, an internal length scale is introduced at the level of the constitutive model. Advanced analyses of localisation phenomena have indicated that constitutive equations with internal length are one solution to model strain localised pattern properly.

The internal length scale is introduced by developing non-local definition of internal variables involved in the material behaviour. The non-local variable $\overset{\circ}{v}$ at a material point x_i can be defined as an averaging value of the local variable v in a considered region Ω near that point [PCB87, PGdBB01], as illustrated in Fig. 1.
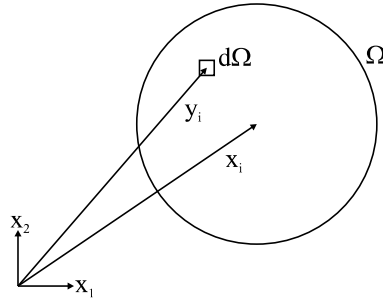

Figure 1: Non-local approach on a representative material volume.

The non-local integral method gives:

$$\overset{\circ}{v}(x_i) = \frac{1}{V} \int\limits_{\Omega} \Psi \, v(y_i) \, d\Omega \tag{1}$$

$$V = \int\limits_{\Omega} \Psi \, d\Omega \tag{2}$$

where x_i is the coordinate vector of the material point where the non-local variable is considered, Ω is a representative volume centred in x_i, y_i is the coordinate vector of the infinitesimal volume $d\Omega$, and Ψ is a weight function scaling $\overset{\circ}{v}$ to $\overset{\circ}{v} = v$ for a homogeneous distribution of the variable. It is generally defined with a Gaussian distribution:

$$\Psi = \frac{1}{(2\pi)^{3/2} \, l_c^3} \, exp \left(-\frac{||x_i - y_i||^2}{2 \, l_c^2} \right) \tag{3}$$

which depends on the distance $||x_i - y_i||$ and on a characteristic length parameter l_c. This length parameter, or internal length scale, defines the material volume that significantly contributes to the non-local variable and is consequently related to the microstructure.

The regularised variable can also be defined explicitly from the local variable $v(x_i)$ and its gradient. In his pioneering works, [Aif84] introduced such gradient in the constitutive equations. The explicit gradient formulation is:

$$\mathring{v} = v + \bar{l}\,\frac{\partial^2 v}{\partial x_i \partial x_i} \tag{4}$$

where the dependence of v and $\mathring{v}$ on the coordinate vector x_i is dropped for simplicity and $\bar{l}$ has the dimension of length squared so $\sqrt{\bar{l}}$ can be related to the internal length scale l_c introduced to regularise the model. Because the gradient term is a local quantity, the spatial interaction of the material points located in the vicinity of $\mathring{v}$ is infinitesimal and the explicit gradient model is therefore local. This is a main difference with the non-local integral formulation of Eq. 1 where the interaction distance is finite and related to the weight function. Moreover, the explicit gradient formulation can be derived from the non-local integral formulation by introducing the gradient of the internal variable, expanding the local variable $v(y_i)$ into a Taylor series [BBC84, LB88, PdBBdV96], using the weight function definition of Eq. 3, and neglecting the terms above the second order (approximation).

The definition of Eq. 4 is less suitable in the context of numerical analyses, such as the finite element method, because of the explicit dependence of $\mathring{v}$ with its local (second) gradient. This dependence leads to a continuity requirement for the internal variable which has to be a continuously differentiable function (class C^1 function whose derivative is continuous). To avoid this drawback, an alternative implicit gradient formulation, introducing an approximation of Eq. 1 similar to Eq. 4, can be expressed as follows [PdBBdV96, PGdBB01]:

$$\mathring{v} - \bar{l}\,\frac{\partial^2 \mathring{v}}{\partial x_i \partial x_i} = v \tag{5}$$

and enables a continuous definition of v (class C^0 function). For the implicit gradient model, the non-local internal variable is an additional unknown which is solution of the Helmoltz differential equation 5. Solution of this equation can only be found provided that additional boundary condition on $\mathring{v}$ is specified. The following condition is usually assumed [LB88]:

$$\frac{\partial \mathring{v}}{\partial x_i}\,n_i = 0 \tag{6}$$

where n_i is the normal unit vector to the external boundary. This condition enables $\mathring{v} = v$ for homogeneous distribution. In contrast to the explicit formulation, the non-local variable $\mathring{v}$ is implicitly given as the solution of Eqs. 5 and 6, and the spatial interaction has a finite distance that implies a non-local character. The solution is of the same form of the non-local equation 1 with $\Psi = Gr$ and $V = 1$, Gr being the Green's function [Zau89]:

$$\mathring{v}(x_i) = \int_\Omega Gr\, v(y_i)\, d\Omega \tag{7}$$

$$Gr = \frac{1}{4\pi \, \bar{l} \, ||x_i - y_i||} \, exp\left(-\frac{||x_i - y_i||}{\sqrt{\bar{l}}}\right) \tag{8}$$

The implicit gradient model is therefore a special case of the non-local model.

Non-local quantities as well as gradient of internal variables can finally be introduced in constitutive models. Among other authors, Bazant, Pijaudier-Cabot, and co-workers [BBC84, PCB87] proposed a family of constitutive models derived from the non-local damage theory in which a non-local internal variable is used instead of the local one. For instance, a non-local damage energy release rate obtained by Eq. 1 is introduced in the damage loading function. Other variables such as non-local equivalent strain are usually used in damage model [PGdBB01].

3.2   Enrichment of the kinematics

The previous approaches (enrichment of the constitutive law) introduce the effect of microstructure with non-local or gradient terms but the microstructure itself is not explicitly defined. To this end, the classical kinematics of a continuous medium can be enriched with additional description of the microstructure kinematics, leading to a microstructure continuum medium also called enriched medium.

For a classical continuous medium, a material particle of volume Ω is defined at macroscopic scale by its (macro) displacement field u_i. The classical kinematic fields are the macro-deformation field:

$$F_{ij} = \frac{\partial u_i}{\partial x_j} \tag{9}$$

corresponding to the gradient of the displacement field, the macro-strain field:

$$\varepsilon_{ij} = \frac{1}{2}\left(F_{ij} + F_{ji}\right) \tag{10}$$

corresponding to the symmetric part of F_{ij}, and the macro-rotation field:

$$r_{ij} = \frac{1}{2}\left(F_{ij} - F_{ji}\right) \tag{11}$$

corresponding to the antisymmetric part of F_{ij}. Their rate forms are also commonly used; the velocity gradient field:

$$L_{ij} = \frac{\partial \dot{u}_i}{\partial x_j} \tag{12}$$

the strain rate field:

$$\dot{\varepsilon}_{ij} = \frac{1}{2}\left(L_{ij} + L_{ji}\right) \tag{13}$$

and the spin rate field:

$$\omega_{ij} = \frac{1}{2}\left(L_{ij} - L_{ji}\right) \tag{14}$$

The first and most famous enhanced model was developed by the Cosserat brothers [CC09] who introduced local rotation degrees of freedom r_i^c in addition to the displacements of classical continua u_i (Fig. 2). The Cosserat (or micropolar) elastic continuum theory is mostly suitable for the kinematic description of granular materials. Accordingly, additional kinematic fields are introduced [VS95]. The deformation due to the particle rotation, also called micro-rotation (antisymmetric tensor) becomes:
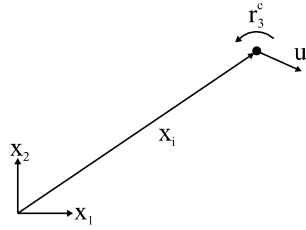

Figure 2: Kinematic degrees of freedom of the Cosserat elastic continuum theory.

$$r_{ij}^c = e_{ijk}\, r_k^c \tag{15}$$

where e_{ijk} is the alternating tensor, and the gradient of the particle rotation, also called curvature:

$$K_{ij}^c = \frac{\partial r_i^c}{\partial x_j} \tag{16}$$

A relative strain is deduced as the difference between macro-deformation and micro-rotation:

$$\overline{\varepsilon}_{ij} = F_{ij} - r_{ij}^c \tag{17}$$

whose symmetric part coincides with the macro-strain ε_{ij} and its antisymmetric part with the difference between the macro and micro-rotation $r_{ij} - r_{ij}^c$. The latter characterises the relative rotation of a material point with regard to the rotation of its neighbourhood. A couple stress (torques) tensor associated to the rotations is thus added introducing bending and torsion at the material point. This results in a moment equilibrium equation involving the couple stresses that comes in addition to the classical (local) momentum balance equation involving the stress field σ_{ij}. Moreover, supplementary elastic constants are considered in the constitutive equations which consist of internal length scale parameters related to the microstructure [VS95].

In the 1960's, [Tou62] and [Min64] defined materials with microstructure. A macro-volume Ω is composed of smaller microscale particles that can be represented by a micro-volume Ω^m, embedded in the material volume Ω (Fig. 3). A micro-displacement field u_i^m is defined independently of the macro-displacement u_i and its gradient leads to a micro-deformation field:

$$\upsilon_{ij} = \frac{\partial u_i^m}{\partial x_j} \tag{18}$$
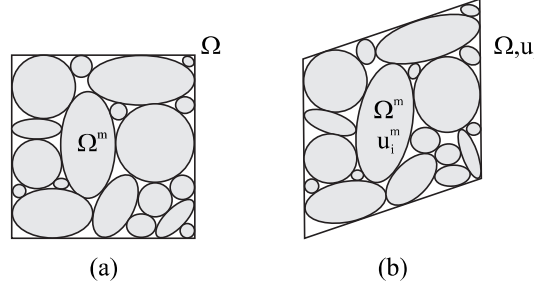
Figure 3: Kinematics of a microstructure continuum: (a) initial configuration and (b) configuration after external solicitation with relative displacement of the microstructure.

which is homogeneous in the micro-volume Ω^m but non-homogeneous in the macro-volume Ω.

The symmetric and antisymmetric parts of υ_{ij} correspond to the micro-strain and micro-rotation:

$$\varepsilon_{ij}^m = \frac{1}{2} \left(\upsilon_{ij} + \upsilon_{ji} \right) \tag{19}$$

$$r_{ij}^m = \frac{1}{2} \left(\upsilon_{ij} - \upsilon_{ji} \right) \tag{20}$$

with the micro-rotation corresponding to the rotation components of the Cosserat model $r_{ij}^m = r_{ij}^c$ (Eq. 15). Cosserat model is in fact a particular case of a microstructure medium. Moreover, the micro second gradient is defined as:

$$h_{ijk} = \frac{\partial \upsilon_{ij}}{\partial x_k} = \frac{\partial^2 u_i^m}{\partial x_j \partial x_k} \tag{21}$$

The relative deformation of the microstructure is defined as the difference between the macro and the micro-deformation fields:

$$\overline{\varepsilon}_{ij} = F_{ij} - \upsilon_{ij} \tag{22}$$

whose symmetric part coincides with the difference between the macro and the micro-strain $\varepsilon_{ij} - \varepsilon_{ij}^m$ and its antisymmetric part with the difference between the macro and micro-rotation $r_{ij} - r_{ij}^m$. Similar to the Cosserat's continuum description, additional stresses are introduced: the microstress, an additive stress field associated to the microstructure, and the double stress.

Later, [Ger73] introduced the virtual power principle to provide a global framework for the microstructure continuum formulation. This principle states that, by equilibrium, the virtual power of all forces acting on a mechanical system is null. In the following, materials with microstructure defined by [Min64] and [Ger73] will be considered.

A large panel of models are developed in the litterature by adding mathematical constraints to microstructure media. Among them, the second gradient model developed in Grenoble [CCH98, CCM01] will be most particularly developed hereafter. Yet, the following conclusions can be generalised to other regularisation techniques.

4   Coupled local second gradient model for microstructure saturated media

The coupled local second gradient model is developed for enriched continua including microstructure effects [CCM01]. This model was extended from monophasic to biphasic porous media (solid and fluid) by [CCC06] to highlight the possible interactions of the fluid (liquid water) with the strain localisation process and with the internal length introduced by the model. The developments proposed by [CCC06] are recalled in this section. They account for a medium with incompressible solid grains, under saturated and isothermal conditions. The solid and fluid phases are considered as immiscible and phase changes, like evaporation and dissolution, are therefore not taken into account.

As for a classical continuum, the material is considered as a porous medium and the balance equations are based on mixture theories. The unknowns of the coupled problem are the macro-displacement u_i, the micro-deformation field v_{ij} (or the micro-displacement field u_i^m by Eq. 18), and the pore water pressure p_w. An additional unknown field of Lagrange multipliers λ_{ij} will be added for the finite element method implementation.
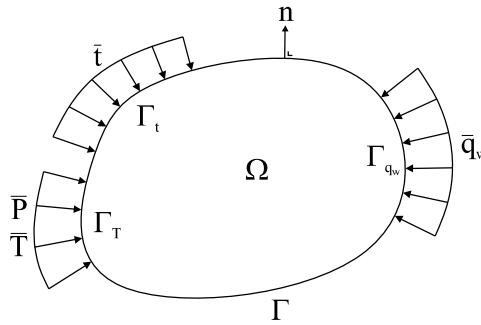

Figure 4: Material system with current configuration Ω and boundary conditions for the second gradient model.

4.1   Balance equations for microstructure poromechanics

4.1.1   Local second gradient model for a monophasic medium

The class of virtual kinematics introduced in the virtual work principle for the classical kinematic theory can be extended in the framework of a microstructure continuum theory, by adding a description of the microstructure kinematics to the classical displacement field. According to Eq. 18, the kinematics at microscale are described by a microkinematic gradient field υ_{ij}. With respect to classical continuum mechanics, additional terms are added in the internal virtual work of a given body [Ger73]. The following expression holds for any virtual quantities:

$$W_{int}^* = \int_{\Omega} \left(\sigma_{ij} \, F_{ij}^* - \tau_{ij} \, \bar{\varepsilon}_{ij}^* + \Sigma_{ijk} \, h_{ijk}^* \right) d\Omega \tag{23}$$

where $\bar{\varepsilon}_{ij}^*$ is the virtual relative deformation of the microstructure:

$$\bar{\varepsilon}_{ij}^* = F_{ij}^* - \upsilon_{ij}^* \tag{24}$$

τ_{ij} is an additional stress associated to the microstructure also called the microstress, $h_{ijk}^* = \dfrac{\partial \upsilon_{ij}^*}{\partial x_k}$ is the virtual micro second gradient, and Σ_{ijk} is the double stress dual of h_{ijk}^*, which needs an additional constitutive law introducing the internal length scale. The external virtual work can be defined as follows:

$$W_{ext}^* = \int_{\Omega} \rho \, g_i \, u_i^* \, d\Omega + \int_{\Gamma_\sigma} \left(\bar{t}_i \, u_i^* + \overline{P}_{ij} \, \upsilon_{ij}^* \right) d\Gamma \tag{25}$$

where $\overline{P}_{ij}$ is an additional external double surface traction acting on a part Γ_T of the boundary Γ (Fig. 4) and $\Gamma_\sigma = \{\Gamma_t \cup \Gamma_T\}$ regroups the classical and additional external solicitations. The virtual work principle assumes the equality between internal and external virtual works and leads to the weak form of the momentum balance equation:

$$\int_{\Omega} \left(\sigma_{ij} \, F_{ij}^* - \tau_{ij} \left(F_{ij}^* - \upsilon_{ij}^* \right) + \Sigma_{ijk} \, h_{ijk}^* \right) d\Omega = \int_{\Omega} \rho \, g_i \, u_i^* \, d\Omega + \int_{\Gamma_\sigma} \left(\bar{t}_i \, u_i^* + \overline{P}_{ij} \, \upsilon_{ij}^* \right) d\Gamma$$

$$\tag{26}$$

The local equilibrium equations are formulated for the macro and the micro quantities; the local momentum balance equations are:

$$\frac{\partial (\sigma_{ij} - \tau_{ij})}{\partial x_j} + \rho \, g_i = 0 \tag{27}$$

$$\frac{\partial \Sigma_{ijk}}{\partial x_k} - \tau_{ij} = 0 \tag{28}$$

and the boundary conditions are:

$$\bar{t}_i = (\sigma_{ij} - \tau_{ij}) \, n_j \tag{29}$$

$$\overline{P}_{ij} = \Sigma_{ijk} \, n_k \tag{30}$$

The boundary conditions for the mixture are also enriched with microstructure effects which leads to non-classical boundary conditions.

In the specific case of local second gradient model used in the following, a kinematic constraint is added in order to obtain a local second gradient continuum medium. No relative deformation of the microstructure is assumed $\bar{\varepsilon}_{ij} = 0$, meaning that the microkinematic gradient is equal to the macro-deformation:

$$\upsilon_{ij} = F_{ij} \tag{31}$$

As a consequence:

$$\upsilon_{ij}^* = F_{ij}^* \tag{32}$$

for the virtual fields. Therefore, the principle of virtual work can be rewritten as follows:

$$\int_{\Omega} \left(\sigma_{ij} \, \frac{\partial u_i^*}{\partial x_j} + \Sigma_{ijk} \, \frac{\partial^2 u_i^*}{\partial x_j \partial x_k} \right) d\Omega = \int_{\Omega} \rho \, g_i \, u_i^* \, d\Omega + \int_{\Gamma_\sigma} \left(\bar{t}_i \, u_i^* + \overline{T}_i \, Du_i^* \right) d\Gamma \tag{33}$$

where $\overline{T}_i$ is the additional external double force per unit area on Γ_T (Fig. 4) and the notation Da denotes the normal derivative of any quantity a:

$$Da = \frac{\partial a}{\partial x_i} \, n_i \tag{34}$$

with:

$$Du_i^* = \frac{\partial u_i^*}{\partial x_j} \, n_j = F_{ij}^* \, n_j = \upsilon_{ij}^* \, n_j \tag{35}$$

The local momentum balance equation reads:

$$\frac{\partial \sigma_{ij}}{\partial x_j} - \frac{\partial^2 \Sigma_{ijk}}{\partial x_j \partial x_k} + \rho \, g_i = 0 \tag{36}$$

and the boundary conditions are:

$$\bar{t}_i = \sigma_{ij} \, n_j - n_k \, n_j \, D\Sigma_{ijk} - \frac{D\Sigma_{ijk}}{Dx_k} \, n_j - \frac{D\Sigma_{ijk}}{Dx_j} \, n_k + \frac{Dn_l}{Dx_l} \, \Sigma_{ijk} \, n_j \, n_k - \frac{Dn_j}{Dx_k} \, \Sigma_{ijk} \tag{37}$$

$$\overline{T}_i = \overline{P}_{ij} \, n_j = \Sigma_{ijk} \, n_j \, n_k \tag{38}$$

where $\frac{Da}{Dx_i}$ is the tangential derivative of any quantity a:

$$\frac{Da}{Dx_i} = \frac{\partial a}{\partial x_i} - \frac{\partial a}{\partial x_j} \, n_j \, n_i \tag{39}$$

The local second gradient possesses the advantage that the constitutive equations remain local, with the stress fields σ_{ij} and Σ_{ijk} being local quantities. A second gradient extension can thenceforward be formulated for any classical continuum mechanics constitutive law.

4.1.2   Second gradient constitutive equation

Similarly to classical media for which a constitutive equation links the stress to the kinematic history, an additional constitutive law has to be defined between the double stress and the microkinematics. The latter is assumed to be decoupled of the classical first gradient part. However, only a little information is available on the relation existing between the double stress and the micro-deformation. A linear elastic mechanical law is chosen for simplicity reasons with the purpose of introducing as few additional parameters as possible. It consists in an isotropic linear relationship involving five independent parameters derived by [Min65]:

$$\tilde{\Sigma}_{ijk} = D_{ijklmn} \frac{\partial \dot{v}_{lm}}{\partial x_n} \tag{40}$$

giving the Jaumann double stress rate:

$$\tilde{\Sigma}_{ijk} = \dot{\Sigma}_{ijk} + \Sigma_{ljk}\,\omega_{li} + \Sigma_{imk}\,\omega_{mj} + \Sigma_{ijp}\,\omega_{pk} \tag{41}$$

as a function of the micro second gradient rate $\dot{h}_{ijk}$. Because the physical meaning of the material parameters composing D_{ijklmn} is not well established, a simplified version introducing only one parameter has been proposed [MCC02]. For two-dimensional problems, it reads:

$$
\begin{bmatrix}
\tilde{\Sigma}_{111} \\
\tilde{\Sigma}_{112} \\
\tilde{\Sigma}_{121} \\
\tilde{\Sigma}_{122} \\
\tilde{\Sigma}_{211} \\
\tilde{\Sigma}_{212} \\
\tilde{\Sigma}_{221} \\
\tilde{\Sigma}_{222}
\end{bmatrix}
= D
\begin{bmatrix}
1 & 0 & 0 & 0 & 0 & \frac{1}{2} & \frac{1}{2} & 0 \\
0 & \frac{1}{2} & \frac{1}{2} & 0 & -\frac{1}{2} & 0 & 0 & \frac{1}{2} \\
0 & \frac{1}{2} & \frac{1}{2} & 0 & -\frac{1}{2} & 0 & 0 & \frac{1}{2} \\
0 & 0 & 0 & 1 & 0 & -\frac{1}{2} & -\frac{1}{2} & 0 \\
0 & -\frac{1}{2} & -\frac{1}{2} & 0 & 1 & 0 & 0 & 0 \\
\frac{1}{2} & 0 & 0 & -\frac{1}{2} & 0 & \frac{1}{2} & \frac{1}{2} & 0 \\
\frac{1}{2} & 0 & 0 & -\frac{1}{2} & 0 & \frac{1}{2} & \frac{1}{2} & 0 \\
0 & \frac{1}{2} & \frac{1}{2} & 0 & 0 & 0 & 0 & 1
\end{bmatrix}
\begin{bmatrix}
\frac{\partial \dot{v}_{11}}{\partial x_1} \\
\frac{\partial \dot{v}_{11}}{\partial x_2} \\
\frac{\partial \dot{v}_{12}}{\partial x_1} \\
\frac{\partial \dot{v}_{12}}{\partial x_2} \\
\frac{\partial \dot{v}_{21}}{\partial x_1} \\
\frac{\partial \dot{v}_{21}}{\partial x_2} \\
\frac{\partial \dot{v}_{22}}{\partial x_1} \\
\frac{\partial \dot{v}_{22}}{\partial x_2}
\end{bmatrix}
\tag{42}
$$

The constitutive elastic parameter D represents the physical microstructure and the internal length scale relevant for the shear band width is related to this parameter [CCH98, KCB$^+$07, CCC09].

4.1.3   Coupled local second gradient model

The second gradient theory was extended from monophasic to biphasic medium by [CCC06]. As for a monophasic medium, microstructure effects have to be introduced in the balance equations of classical poromechanics.

The linear momentum balance equation is identical to Eq. 33:

$$\int_{\Omega} \left(\sigma_{ij}\, \frac{\partial u_i^*}{\partial x_j} + \Sigma_{ijk}\, \frac{\partial^2 u_i^*}{\partial x_j \partial x_k} \right) d\Omega = \int_{\Omega} \rho\, g_i\, u_i^*\, d\Omega + \int_{\Gamma_{\sigma}} \left(\bar{t}_i\, u_i^* + \overline{T}_i\, Du_i^* \right) d\Gamma \quad (43)$$

The water mass balance equation is written, in a weak form, in a similar way as the momentum balance equation. A kinematically admissible virtual pore water pressure field p_w^* is considered and is involved, as well as its first derivative, in the internal and external virtual quantities. The water mass balance equation reads:

$$\int_{\Omega} \left(\dot{M}_w\, p_w^* - f_{w,i}\, \frac{\partial p_w^*}{\partial x_i} \right) d\Omega = \int_{\Omega} Q_w\, p_w^*\, d\Omega - \int_{\Gamma_{q_w}} \bar{q}_w\, p_w^*\, d\Gamma \quad (44)$$

where M_w is the water mass inside Ω, $f_{w,i}$ is the water mass flow, Q_w is a sink term of water mass, and $\bar{q}_w$ is the input water mass (positive for inflow) per unit area on a part Γ_{q_w} of Γ (Fig. 4).

According to the previous assumptions, the momentum balance equation Eq. 33 remains valid provided ρ and σ_{ij} are defined, knowing that the medium is a mixture of a solid phase and one fluid.

The mixture homogenised mass density is given by:

$$\rho = \rho_s\, (1 - \Phi) + \rho_w\, \Phi \quad (45)$$

and the effective stress is defined according to the Terzaghi's postulate:

$$\sigma_{ij} = \sigma'_{ij} + p_w\, \delta_{ij} \quad (46)$$

Furthermore, it is assumed that the pore fluid does not have an influence at microscale; therefore, pore water pressure variations do not generate microkinematic gradients. Such additional hypothesis was formulated by Ehlers [EV98] on a Cosserat model for a biphasic medium. Second gradient effects are only assumed for the solid phase and the water mass balance equation Eq. 44 of classical poromechanics is conserved. The governing equations of the coupled problem are therefore Eqs. 33 and 44.

As already mentioned for the classical poromechanics, the effect of water on the total stress is defined according to the effective stress postulate (Eq. 46) while on the

contrary the double stress Σ_{ijk} is independent of the pore water pressure. The double stress is only related to the solid phase.

The water mass M_w inside Ω and the water mass flow $f_{w,i}$ are defined in the following equations:

$$M_w = \rho_w \, \Phi \, \Omega \tag{47}$$

$$f_{w,i} = -\rho_w \, \frac{k_w}{\mu_w} \left(\frac{\partial p_w}{\partial x_i} + \rho_w \, g_i \right) \tag{48}$$

The definitions of the phase density variations and of the porosity evolution are:

$$\frac{\dot{\rho}_w}{\rho_w} = \frac{\dot{p}_w}{\chi_w} \tag{49}$$

$$\dot{\rho}_s = 0 \tag{50}$$

$$\dot{\Phi} = (1 - \Phi) \, \frac{\dot{\Omega}}{\Omega} \tag{51}$$

The latter lead to the time derivative of the water mass per unit mixture volume:

$$\dot{M}_w = \rho_w \left(\frac{\dot{p}_w}{\chi_w} \, \Phi + \frac{\dot{\Omega}}{\Omega} \right) \tag{52}$$

4.2   Coupled finite element formulation

4.2.1   Numerical implementation

The virtual work formulation of second gradient models can be implemented in a finite element code. To implement the momentum balance equation of Eq. 33, the displacement field has to be a continuously differentiable function because second order derivatives of the displacement field are involved [ZPV01b]. To avoid the use of C1 function, the kinematic restrictions $\upsilon_{ij} = F_{ij}$ and $\upsilon_{ij}^* = F_{ij}^*$ are introduced in the momentum balance equation through a field of Lagrange multipliers λ_{ij} related to a weak form of the constraint [CCH98]. The field equations of the numerical coupled problem are:

$$\int_{\Omega^t} \left(\sigma_{ij}^t \, \frac{\partial u_i^*}{\partial x_j^t} + \Sigma_{ijk}^t \, \frac{\partial \upsilon_{ij}^*}{\partial x_k^t} \right) d\Omega^t - \int_{\Omega^t} \lambda_{ij}^t \left(\frac{\partial u_i^*}{\partial x_j^t} - \upsilon_{ij}^* \right) d\Omega^t = \int_{\Omega^t} \rho^t \, g_i \, u_i^* \, d\Omega^t + \int_{\Gamma_\sigma^t} \left(\bar{t}_i^t \, u_i^* + \bar{T}_i^t \, \upsilon_{ik}^* \, n_k^t \right) d\Gamma^t$$

$$\tag{53}$$

$$\int_{\Omega^t} \lambda_{ij}^* \left(\frac{\partial u_i^t}{\partial x_j^t} - \upsilon_{ij}^t \right) d\Omega^t = 0 \tag{54}$$

$$\int_{\Omega^t} \left(\dot{M}_w^t \, p_w^* - f_{w,i}^t \, \frac{\partial p_w^*}{\partial x_i^t} \right) d\Omega^t = \int_{\Omega^t} Q_w^t \, p_w^* \, d\Omega^t - \int_{\Gamma_{qw}^t} \bar{q}_w^t \, p_w^* \, d\Gamma^t \tag{55}$$

where the notation a^t corresponds to the current value of any quantity a for a given time t. For boundary conditions problems, the virtual quantities included in the above equations depend on the boundary conditions history. Thus, the governing equations and the constitutive equations have to hold at any time t.

4.2.2 Linearisation of the field equations

Solving the loading process of a boundary conditions problem consists in determining the unknown fields u_i, υ_{ij}, λ_{ij}, and p_w for which the equilibrium equations 53, 54, and 55 are valid. Since this system of non-linear equations is *a priori* not verified for any instant t, the problem is numerically solved by iterative procedure. It involves a time discretisation over finite time steps Δt:

$$\tau = t + \Delta t \tag{56}$$

and an implicit scheme of finite differences for the rate of any quantity a:

$$\dot{a}^\tau = \frac{a^\tau - a^t}{\Delta t} \tag{57}$$

A full Newton-Raphson method is used to find a solution for the new fields u_i, υ_{ij}, λ_{ij}, and p_w at the end of each time step which is in equilibrium with the boundary conditions.

Following the approach of [BA95], the method aims to define a linear auxiliary problem deriving from the continuum one. A first configuration Ω^t in equilibrium with the boundary conditions at a given time t is assumed to be known and another Ω^τ in equilibrium at the end of the time step $\tau = t + \Delta t$ has to be found. The aim of the iterative numerical procedure is to determine this new configuration at the end of the time step. Firstly, a configuration which is close to the solution but not at equilibrium is guessed and denoted as $\Omega^{\tau 1}$. Both configurations at time t and $\tau 1$ are assumed to be known and non-equilibrium forces for the three considered equations, i.e. the residuals $\Delta_1^{\tau 1}$, $\Delta_2^{\tau 1}$, and $\Delta_3^{\tau 1}$, are defined. The objective is to find another configuration $\Omega^{\tau 2}$ close to $\Omega^{\tau 1}$ for which the non-equilibrium forces vanish. To obtain the linear auxiliary problem, the field equations for $\Omega^{\tau 2}$ are subtracted from the field equations in configuration $\Omega^{\tau 1}$, after being rewritten in configuration $\Omega^{\tau 1}$ by using the Jacobian matrix of the transformation between the two configurations:

$$\overline{F}_{ij} = \frac{\partial x_i^{\tau 2}}{\partial x_j^{\tau 1}} \tag{58}$$

and its Jacobian determinant:

$$det(F) = \left| \frac{\partial x_i^{\tau 2}}{\partial x_j^{\tau 1}} \right| \tag{59}$$

Assuming that g_i, $\bar{t}_i$, $\bar{q}_w$, and Q_w are independent of the different unknown fields (displacement and pore water pressure), and that $\overline{T}_i$ vanishes give:

$$\int_{\Omega^{\tau 1}} \frac{\partial u_i^*}{\partial x_l^{\tau 1}} \left(\sigma_{ij}^{\tau 2} \frac{\partial x_l^{\tau 1}}{\partial x_j^{\tau 2}} det(F) - \sigma_{il}^{\tau 1} \right) + \frac{\partial v_{ij}^*}{\partial x_l^{\tau 1}} \left(\Sigma_{ijk}^{\tau 2} \frac{\partial x_l^{\tau 1}}{\partial x_k^{\tau 2}} det(F) - \Sigma_{ijl}^{\tau 1} \right) d\Omega^{\tau 1}$$

$$- \int_{\Omega^{\tau 1}} \frac{\partial u_i^*}{\partial x_l^{\tau 1}} \left(\lambda_{ij}^{\tau 2} \frac{\partial x_l^{\tau 1}}{\partial x_j^{\tau 2}} det(F) - \lambda_{il}^{\tau 1} \right) - v_{ij}^* \left(\lambda_{ij}^{\tau 2} det(F) - \lambda_{ij}^{\tau 1} \right) d\Omega^{\tau 1} \tag{60}$$

$$- \int_{\Omega^{\tau 1}} u_i^* \left(\rho^{\tau 2} det(F) - \rho^{\tau 1} \right) g_i \, d\Omega^{\tau 1} = -\Delta_1^{\tau 1}$$

$$\int_{\Omega^{\tau 1}} \lambda_{ij}^* \left(\left(\frac{\partial u_i^{\tau 2}}{\partial x_k^{\tau 1}} \frac{\partial x_k^{\tau 1}}{\partial x_j^{\tau 2}} det(F) - \frac{\partial u_i^{\tau 1}}{\partial x_j^{\tau 1}} \right) - \left(v_{ij}^{\tau 2} det(F) - v_{ij}^{\tau 1} \right) \right) d\Omega^{\tau 1} = -\Delta_2^{\tau 1} \tag{61}$$

$$\int_{\Omega^{\tau 1}} p_w^* \left(\dot{M}_w^{\tau 2} det(F) - \dot{M}_w^{\tau 1} \right) - \frac{\partial p_w^*}{\partial x_l^{\tau 1}} \left(f_{w,i}^{\tau 2} \frac{\partial x_l^{\tau 1}}{\partial x_i^{\tau 2}} det(F) - f_{w,l}^{\tau 1} \right) d\Omega^{\tau 1} = -\Delta_3^{\tau 1} \tag{62}$$

By making the two configurations tend towards each other, the variations between them can be defined for any quantity a as:

$$da^{\tau 1} = a^{\tau 2} - a^{\tau 1} \tag{63}$$

The balance equations can be rewritten by taking into account these variations. The complete development of the linearisation of the field equation system and of the resulting linear auxiliary problem is exposed by [CCC06].

4.2.3   Spatial discretisation

In finite element methods, each continuum body is discretised by finite elements and the above field equations are spatially discretised. For the second gradient model, the discretisation is realised by two-dimensional plane-strain isoparametric finite elements. These elements are composed of eight nodes for the displacement field u_i and

the pore water pressure p_w, four nodes for the microkinematic gradient field υ_{ij}, and one node for the Lagrange multiplier field λ_{ij} (Fig. 5). Quadratic serendipity shape functions [ZT00] are used for the u_i and p_w interpolations, linear shape functions are used for υ_{ij}, whereas λ_{ij} is assumed constant.
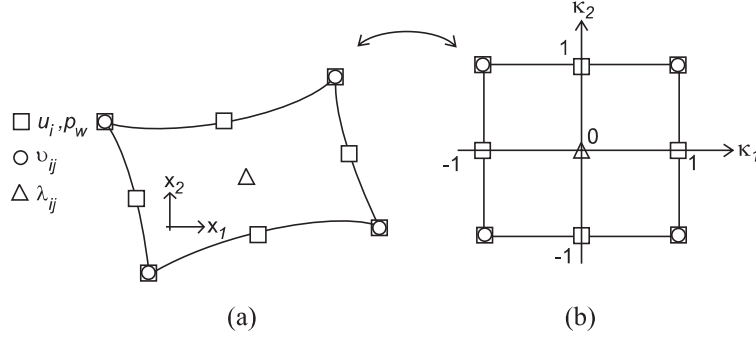

Figure 5: Finite element used for the spatial discretisation of the coupled local second gradient model: (a) current quadrilateral element and (b) parent element [CCC06].

The balance equations of the coupled finite element problem (linear auxiliary problem) have to be rewritten in matricial form to define the local stiffness matrix of an element:

$$\int_{\Omega^{\tau1}} \left[U^{*,\tau1}_{(x_1,x_2)} \right]^T \left[E^{\tau1} \right] \left[dU^{\tau1}_{(x_1,x_2)} \right] d\Omega^{\tau1} = -\Delta_1^{\tau1} - \Delta_2^{\tau1} - \Delta_3^{\tau1} \tag{64}$$

where $\left[dU^{\tau1}_{(x_1,x_2)} \right]$ is the vector of the unknown increments of nodal variables in the current element configuration:

$$\left[dU^{\tau1}_{(x_1,x_2)} \right]_{25\times1} = \left[\frac{\partial du_1^{\tau1}}{\partial x_1^{\tau1}} \ \frac{\partial du_1^{\tau1}}{\partial x_2^{\tau1}} \ \frac{\partial du_2^{\tau1}}{\partial x_1^{\tau1}} \ \frac{\partial du_2^{\tau1}}{\partial x_2^{\tau1}} \ du_1^{\tau1} \ du_2^{\tau1} \ \frac{\partial dp_w^{\tau1}}{\partial x_1^{\tau1}} \ \frac{\partial dp_w^{\tau1}}{\partial x_2^{\tau1}} \ dp_w^{\tau1} \ \frac{\partial d\upsilon_{11}^{\tau1}}{\partial x_1^{\tau1}} \ \frac{\partial d\upsilon_{11}^{\tau1}}{\partial x_2^{\tau2}} \right.$$

$$\left. \frac{\partial d\upsilon_{12}^{\tau1}}{\partial x_1^{\tau1}} \ ... \ \frac{\partial d\upsilon_{22}^{\tau1}}{\partial x_2^{\tau1}} \ d\upsilon_{11}^{\tau1} \ d\upsilon_{12}^{\tau1} \ d\upsilon_{21}^{\tau1} \ d\upsilon_{22}^{\tau1} \ d\lambda_{11}^{\tau1} \ d\lambda_{12}^{\tau1} \ d\lambda_{21}^{\tau1} \ d\lambda_{22}^{\tau1} \right]^T \tag{65}$$

$\left[U^{*,\tau1}_{(x_1,x_2)} \right]$ is a vector having the same structure with the corresponding virtual quantities:

$$\left[U^{*,\tau1}_{(x_1,x_2)} \right]_{1\times25} = \left[\frac{\partial u_1^*}{\partial x_1^{\tau1}} \ \frac{\partial u_1^*}{\partial x_2^{\tau1}} \ \frac{\partial u_2^*}{\partial x_1^{\tau1}} \ \frac{\partial u_2^*}{\partial x_2^{\tau1}} \ u_1^* \ u_2^* \ \frac{\partial p_w^*}{\partial x_1^{\tau1}} \ \frac{\partial p_w^*}{\partial x_2^{\tau1}} \ p_w^* \ \frac{\partial \upsilon_{11}^*}{\partial x_1^{\tau1}} \ \frac{\partial \upsilon_{11}^*}{\partial x_2^{\tau2}} \right.$$

$$\left. \frac{\partial \upsilon_{12}^*}{\partial x_1^{\tau1}} \ ... \ \frac{\partial \upsilon_{22}^*}{\partial x_2^{\tau1}} \ \upsilon_{11}^* \ \upsilon_{12}^* \ \upsilon_{21}^* \ \upsilon_{22}^* \ \lambda_{11}^* \ \lambda_{12}^* \ \lambda_{21}^* \ \lambda_{22}^* \right] \tag{66}$$

and $\left[E^{\tau 1} \right]$ is the current element stiffness (tangent) matrix defined as follows:

$$
\left[E^{\tau 1} \right]_{25 \times 25} =
\begin{bmatrix}
E^{\tau 1}_{1_{4 \times 4}} & 0_{4 \times 2} & K^{\tau 1}_{WM_{4 \times 3}} & 0_{4 \times 8} & 0_{4 \times 4} & -I_{4 \times 4} \\
G^{\tau 1}_{1_{2 \times 4}} & 0_{2 \times 2} & G^{\tau 1}_{2_{2 \times 3}} & 0_{2 \times 8} & 0_{2 \times 4} & 0_{2 \times 4} \\
K^{\tau 1}_{MW_{3 \times 4}} & 0_{3 \times 2} & K^{\tau 1}_{WW_{3 \times 3}} & 0_{3 \times 8} & 0_{3 \times 4} & 0_{3 \times 4} \\
E^{\tau 1}_{2_{8 \times 4}} & 0_{8 \times 2} & 0_{8 \times 3} & D^{\tau 1}_{8 \times 8} & 0_{8 \times 4} & 0_{8 \times 4} \\
E^{\tau 1}_{3_{4 \times 4}} & 0_{4 \times 2} & 0_{4 \times 3} & 0_{4 \times 8} & 0_{4 \times 4} & I_{4 \times 4} \\
E^{\tau 1}_{4_{4 \times 4}} & 0_{4 \times 2} & 0_{4 \times 3} & 0_{4 \times 8} & -I_{4 \times 4} & 0_{4 \times 4}
\end{bmatrix}
\tag{67}
$$

The matrices $\left[E^{\tau 1}_1 \right]$, $\left[E^{\tau 1}_2 \right]$, $\left[E^{\tau 1}_3 \right]$, $\left[E^{\tau 1}_4 \right]$, and $\left[D^{\tau 1} \right]$ are the same as the ones used in the local second gradient model for monophasic medium by [CM04] ($\left[D^{\tau 1} \right] = D_{ijklmn}$ in Eqs. 40 and 42). $\left[K^{\tau 1}_{WW} \right]$ is the classical stiffness matrix of a flow problem, $\left[K^{\tau 1}_{MW} \right]$ and $\left[K^{\tau 1}_{WM} \right]$ are matrices of the coupling between the flow and the mechanical problems detailed by [CCC06]. Moreover, $\left[G^{\tau 1}_1 \right]$ and $\left[G^{\tau 1}_2 \right]$ are related to the contribution of gravity volume force.

The finite element spatial discretisation of the linear auxiliary problem is introduced in Eq. 64 by using transformation matrices $\left[T^{\tau 1} \right]$ and $[B]$ that connect the current element vector $\left[dU^{\tau 1}_{(x_1, x_2)} \right]$ to the parent element vector $\left[dU^{\tau 1}_{(\kappa_1, \kappa_2)} \right]$ and to the nodal variables $\left[dU^{\tau 1}_{Node} \right]$:

$$
\left[dU^{\tau 1}_{(x_1, x_2)} \right] = \left[T^{\tau 1} \right] \left[dU^{\tau 1}_{(\kappa_1, \kappa_2)} \right] = \left[T^{\tau 1} \right] [B] \left[dU^{\tau 1}_{Node} \right]
\tag{68}
$$

The matrices $[B]$ and $\left[T^{\tau 1} \right]$ contain the interpolation functions and their derivatives. Moreover, the vector $\left[U^{*, \tau 1}_{(x_1, x_2)} \right]$ is related to $\left[U^{*, \tau 1}_{Node} \right]$ in the same manner.

The integration in Eq. 64 can be expressed for each parent element as follows:

$$
\int_{\Omega^{\tau 1}} \left[U^{*, \tau 1}_{(x_1, x_2)} \right]^T \left[E^{\tau 1} \right] \left[dU^{\tau 1}_{(x_1, x_2)} \right] d\Omega^{\tau 1} = \left[U^{*, \tau 1}_{Node} \right]^T \left[k^{\tau 1} \right] \left[dU^{\tau 1}_{Node} \right]
\tag{69}
$$

where $\left[k^{\tau 1} \right]$ is the local element stiffness matrix:

$$
\left[k^{\tau 1} \right] = \int_{-1}^{1} \int_{-1}^{1} [B]^T \left[T^{\tau 1} \right]^T \left[E^{\tau 1} \right] \left[T^{\tau 1} \right] [B] \, det(J^{\tau 1}) \, d\kappa_1 \, d\kappa_2
\tag{70}
$$

with $det(J^{\tau 1})$ the determinant of the Jacobian matrix of the transformation between the parent (κ_1, κ_2) and the current (x_1, x_2) elements:

$$
det(J^{\tau 1}) = \left| \frac{\partial x^{\tau 1}_i}{\partial \kappa_j} \right|
\tag{71}
$$

The residual terms are also computed locally for each element and define the elementary out of balance force vector $\left[f_{OB}^{\tau 1}\right]$:

$$-\Delta_1^{\tau 1} - \Delta_2^{\tau 1} - \Delta_3^{\tau 1} = \left[U_{Node}^{*,\tau 1}\right]^T \left[f_{OB}^{\tau 1}\right] \tag{72}$$

4.2.4 Global solution

Once the elementary stiffness matrices and out of balance force vectors are computed, they are assembled to obtain the global stiffness matrix $\left[K^{\tau 1}\right]$ and the global out of balance force vector $\left[F_{OB}^{\tau 1}\right]$ of the whole continuum. The linear auxiliary system is solved by computing:

$$\left[K^{\tau 1}\right]\left[\delta U_{Node}^{\tau 1}\right] = -\left[F_{OB}^{\tau 1}\right] \tag{73}$$

where $\left[\delta U_{Node}^{\tau 1}\right]$ is the global correction vector of the nodal degrees of freedom. The current configuration is actualised by adding the corrections to their respective current values. The new current configuration is closer to the well-balanced configuration and its equilibrium is checked, leading to a new iteration or to the end of the loading step of the iterative procedure.

4.3 Two-dimensional specimen under compression

A finite element modelling of two-dimensional plane-strain compression tests is first considered. These tests have been widely reproduced on small-scale specimens to emphasise the strain localisation effects.

Among various authors, the results obtained by [CLC09] for a uniaxial compression are principally developed hereafter. A sketch of the boundary value problem in plane-strain state is illustrated in Fig. 6. The vertical displacement u_a of the sample upper surface (smooth and rigid boundary) is progressively increased during the test with a constant loading strain rate to model the vertical compression. The vertical displacement of the bottom surface is blocked (rigid boundary) and the displacement of the central node is blocked in both directions to avoid rigid body displacement.

4.3.1 Classical medium

A mechanical modelling is presetned hereafter for a classical medium (without a regularization method). The (first gradient) constitutive law is an elastoplastic strain-softening model in an associated softening plasticity framework ($\varphi = \psi$, $F^p = G^p$): a Drucker-Prager yield criterion is considered with no hardening of the friction angle, and a cohesion softening function [CLC09].

A homogeneous response of the specimen is first studied. The global response is detailed in Fig. 7 (a) where one can observe a linear elastic behaviour, then a non-linear
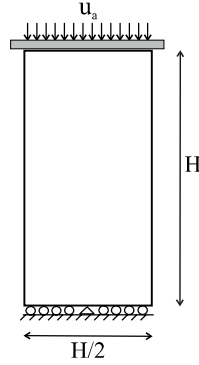
Figure 6: Sketch of the plane-strain compression test.

plastic behaviour before the peak stress including cohesion softening, and finally a plastic behaviour with decrease of the global load response. Concerning the orientation of the shear band, the Rice criterion gives the orientation of the first possible shear band occurrence [RR75],[Ric76]. This criterion can be used for a single-mechanism elastoplastic model such as the studied problem. The Rice criterion $det(\wedge_{jk})$ evolution is presented during the increasing loading history in Fig. 7 (b) as a function of $tan\Theta$, $\wedge_{jk}$ is the Acoustic tensor and Θ is the orientation of the shear band normal to the loading vertical axis, i.e. the shear band orientation with the horizontal direction. The criterion is positive $det(\wedge_{jk} > 0)$ as long as the behaviour is elastic and even for an elastoplastic loading until the first bifurcation is predicted $(det(\wedge_{jk}) = 0)$. For a certain load, the bifurcation criterion is met at every material point and two symmetric (conjugate) bifurcation directions are predicted with an orientation of $\Theta = \pm60°$. This bifurcation point corresponds to the peak stress on the global response curve and to the start of the load response reduction in associated plasticity. A range of possible orientations is predicted for an increasing load corresponding to a multitude of possible solutions $(det(\wedge_{jk}) <= 0)$.

For a perfect sample, although softening plasticity is considered, the strain localisation is not automatically triggered and the numerical solution may remain homogeneous even after the bifurcation criterion is met. In reality, the localisation process is generated because geomaterials exhibit heterogeneities. Different numerical procedures are available to force the occurrence of strain localisation. The most used one is the introduction of an imperfection, such as disturbing force, material imperfection, or geometrical defect [CRB97, MCC02, ZSS01]. The modification of numerical parameters, such as time step size and sequences can also be performed [MSC14, SaHC09]. A third method that will be discussed later is a random initialisation of variables [CCC01].

Among these procedures, [CLC09] introduced a material imperfection in the bottom left finite element of the sample under compression. Initially the strain field in the
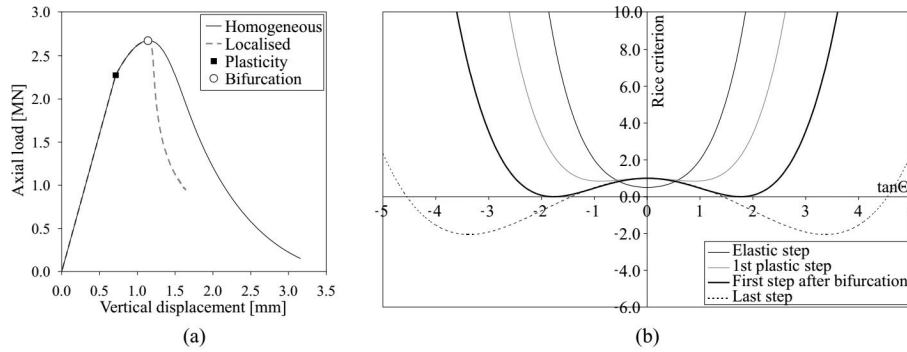
Figure 7: Uniaxial compression: (a) global specimen response curves and (b) Rice criterion at several loading steps for the homogeneous solution [CLC09].

sample is homogeneous, and once the bifurcation criterion is met, the imperfection instigates the development of a shear band across the specimen. The strain localisation as well as its dependency to the mesh size is illustrated in Fig. 8 for a classical medium. The localised solution is therefore non-homogeneous, with the shear band under plastic loading and the outer material under elastic unloading. The global sample response is detailed in Fig. 7 (a) where a rapid decrease of the global reaction is observed once the shear band establishes. The shear band appearance corresponds therefore to the curve peak load (or peak stress) as concluded from laboratory evidences in section 2. The latter also indicate that a material inclusion can act as a strain localisation attractor, which is confirmed by the numerical results. The non-uniqueness issue of the problem after the bifurcation point has consequently been addressed by the imperfection inclusion which leads to one post-bifurcation solution.
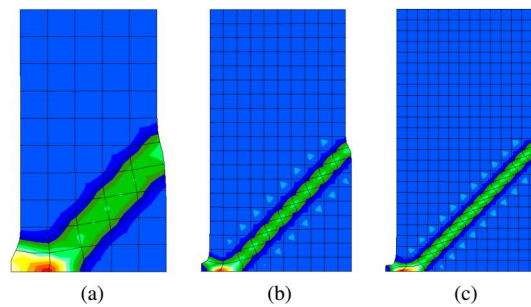
Figure 8: Localised patterns represented by the deviatoric deformation for classical medium: finite element meshes of (a) 50, (b) 190, and (c) 325 elements.

4.3.2   Microstructure enhanced medium

To fix the pathological mesh sensitivity, an enhanced microstructure medium is used. More specifically, the local second gradient medium is adopted, with the second gradient constitutive law given by Eq. 42. The strain localisation pattern induced by the imperfection is illustrated in Fig. 9 with the Gauss integration points under softening plastic loading shown as red squares. This representation permits to measure the shear band width and to notice that it stays constant no matter the element size, implying that the shear strain localisation is mesh-independent. Thus, the strain localisation is correctly regularised thanks to the internal length scale introduced by the second grade model. This is also the case for unstructured mesh [BCC06] and for a biphasic porous medium under saturated conditions, using the coupled local second gradient model [CCC06].

(a)   (b)   (c)
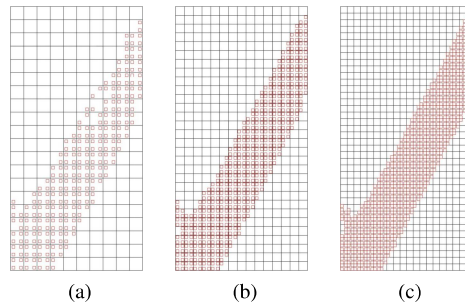
Figure 9: Localised patterns represented by the plastic zone for a second gradient medium: finite element meshes of (a) 200, (b) 450, and (c) 800 elements.

However, the regularisation of the strain localisation process is satisfactory, provided that the second gradient elastic modulus D is calibrated properly to represent the shear bands properly. As already mentioned, the internal length scale inherent to the second gradient mechanical law is related to this constitutive parameter. The value of D should be therefore evaluated based on experimental measurements of shear band thickness for the considered material. From a modelling point of view, a better numerical prediction of the post-localisation plastic behaviour within the bands is obtained if at least three elements compose the shear band width [BCC06]. This remark is valid for any regularisation technique including the second gradient model but also gradient plasticity and non-local models.

4.3.3   Non-uniqueness of the solution

The non-uniqueness of the post-peak solution of an initial boundary value problem can be studied using special numerical techniques. In fact, instead of using a material

imperfection, localised solutions can be found for a homogeneous material using a random initialisation of the strain rate field (nodal velocities) or of material characteristics at the beginning of the iterative procedure. This technique has been mainly proposed by Chambon and co-workers [CCC01] who developed an algorithm to search several possible localised solutions by random initialisation. This algorithm has been adapted to the second-gradient models by [CM04].

Numerical modelling of compression tests performed with the second gradient model illustrates the non-uniqueness of localised solutions of the same initial boundary value problem [BCC06]. The random initialisation is adopted for the increment of nodal quantities $\left[dU_{Node}^{\tau 1}\right]$ (Eq. 68) related to the values obtained at the end of the preceding time step. The obtained non-homogeneous solutions are detailed in Fig. 10 (a) where the different solutions exhibit one to three bands with a possible reflection on the top and bottom faces of the sample because of the imposed vertical displacement. The results indicate that the band thickness is reproducible even if the localisation pattern is different in terms of bands position and number.

As before, the strain localisation occurring at the bifurcation point is due to the strain softening behaviour and possible elastic unloading. Fig. 10 (b) illustrates the global response curves that are different of those in Fig. 7 because a different first gradient law is used. These curves are grouped in packages characterised by the number of deformation bands. It is evident that the higher the band number, the closer the curves are to the homogeneous plastic case. A similar conclusion was drawn from the bar in traction studied by [CCH98], [JKC14].

4.3.4   Bifurcation criterion for the second gradient model

A bifurcation analysis applied to the second gradient model is proposed by [BCC06]. The authors indicate that the bifurcation criterion of the second gradient model is, as for a classical medium, a necessary but not sufficient condition for the localisation onset and that it is met after the bifurcation criterion of the classical medium is verified. Thus, the bifurcation analysis reduces to an analysis on the classical part of the constitutive model.

5   Coupled local second gradient model for an unsaturated medium

The procedure to extend the local second gradient model in saturated conditions to other multiphysical contexts is more or less the same: additional balance equations have to be considered to model the other processes. The main issue is not a numerical one but rather a physical one. What are the possible interactions between the second gradient model and the thermal diffusion, the suction or the chemical reaction? These
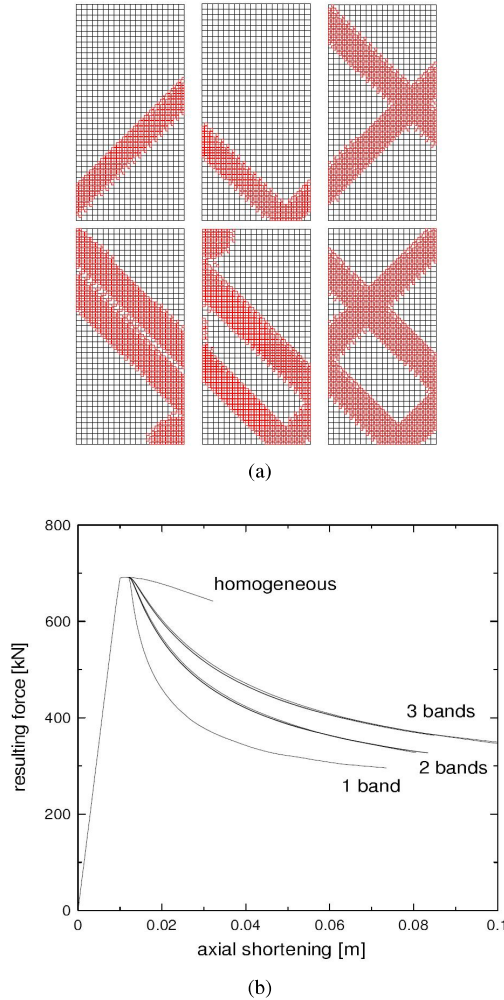
(a)

(b)

Figure 10: Example of localised solutions for a compression test obtained after a random initialisation: (a) plastic zone and (b) global response curve [BCC06].

questions should be first addressed by experimental campaigns. Concerning the internal length introduced by the second gradient model, it comes as the ratio of two constitutive moduli: the one related to the second gradient constitutive law and the one related to the classical law [CCH98]. Considering that the classical constitutive moduli are influenced by the different processes (chemical, thermal, suction ...), the conclusions should be that the internal length scale should be modified by these latter processes (under the condition that second gradient law is not influenced by the processes). This should be again confirmed by some experimental evidences!

The coupled local second gradient model developed by [CCC06] for a biphasic porous medium can be extended to unsaturated materials with compressible solid grains. Hereafter, the unsaturated conditions are taken into account and the compressibility of the solid grains is introduced through the Biot's coefficient. Additionally, the permeability anisotropy is incorporated in the model to better represent the water flows, even if the mechanical behaviour remains isotropic.

5.1   Partial saturation conditions

For unsaturated conditions the water mass inside a porous material volume Ω corresponds to:

$$M_w = \rho_w\, \Phi\, S_{r,w}\, \Omega \tag{74}$$

and its time derivative corresponds to:

$$\dot{M}_w = \dot{\rho}_w\, \Phi\, S_{r,w}\, \Omega + \rho_w\, \dot{\Phi}\, S_{r,w}\, \Omega + \rho_w\, \Phi\, \dot{S}_{r,w}\, \Omega + \rho_w\, \Phi\, S_{r,w}\, \dot{\Omega} \tag{75}$$

This amount of water, which depends on the degree of water saturation $S_{r,w}$, leads to the following mixture homogenised mass density:

$$\rho = \rho_s\, (1 - \Phi) + S_{r,w}\, \rho_w\, \Phi \tag{76}$$

and the water advective flow for anisotropic hydraulic permeability is given by Darcy's law:

$$f_{w,i} = -\rho_w\, \frac{k_{w,ij}\, k_{r,w}}{\mu_w}\, \left(\frac{\partial p_w}{\partial x_j} + \rho_w\, g_j \right) \tag{77}$$

where $k_{r,w}$ is the water relative permeability.

The fluid mass and fluid flows are mostly governed by the water retention property of the material and by its hydraulic permeability. Both of them are related to the partial water saturation and a relative permeability coefficient is introduced in the generalised Darcy's law. Among various possible analytical expressions, the water retention and relative permeability curves are given by van Genuchten's and Mualem's models [Mua76, vG80]:

$$S_{r,w} = S_{res} + (S_{max} - S_{res}) \left(1 + \left(\frac{p_c}{P_r} \right)^{\frac{1}{1-\mathcal{M}}} \right)^{-\mathcal{M}} \tag{78}$$

$$k_{r,w} = \sqrt{S_{r,w}} \left(1 - \left(1 - S_{r,w}^{\frac{1}{\mathcal{M}}} \right)^{\mathcal{M}} \right)^2 \tag{79}$$

where P_r is the air entry pressure, S_{max} and S_{res} are the maximum and residual water degrees of saturation, $\mathcal{M}$ is a model coefficient, and p_c is the capillary pressure.

5.2   Anisotropy of the intrinsic permeability

The advective flow of water (Eq. 77) depends on the anisotropic characteristics of the material through the anisotropic intrinsic permeability. For anisotropic materials and by symmetry of the tensor, the intrinsic permeability tensor $k_{w,ij}$ requires six components to describe the flow characteristics. However, materials commonly exhibit limited forms of anisotropy and stratified geomaterials require only two parameters for the description of the water flow. For horizontal layering in the plane (x_1,x_3), the intrinsic hydraulic permeability tensor is defined with the horizontal and vertical permeabilities, $k_{w,h}$ and $k_{w,v}$, as follows:

$$k_{w,ij} = \begin{bmatrix} k_{w,h} & 0 & 0 \\ 0 & k_{w,v} & 0 \\ 0 & 0 & k_{w,h} \end{bmatrix} \tag{80}$$

5.3   Compressibility of the solid grains

The material compressibility is defined within the scope of poroelasticity [DC93] and is based on the different compressibilities of a porous material. Those are: the compressibility of the bulk material C (solid skeleton), the compressibility of the pores C_p, and the compressibility of the solid phase C_s (rock matrix) with $C_s < C$. The different types of compressibility induce different behaviours of the rock matrix and of the porous material. They can deform differently and the porous material may enter plastic state while the solid grains remain elastic. In the general Biot framework [Bio41], the Biot's coefficient is expressed by:

$$b = \frac{\Phi\, C_p}{C} = 1 - \frac{K}{K_s} \tag{81}$$

as a function of the drained bulk modulus of the material K and the bulk modulus of the solid phase K_s. This coefficient represents the relative deformability of the solid grains with regard to the solid skeleton [Bio41, BW57, Ske60]. Biot proposed for the effective stress definition to use b as a scaling factor that reduces the effect of p_w on σ_{ij} due to a reduction of pore compressibility. The Biot's stress definition can be formulated under unsaturated conditions presuming that the assumptions on compressibility hold under these conditions [NL08]:

$$\sigma_{ij} = \sigma'_{ij} - b\, S_{r,w}\, p_w\, \delta_{ij} \tag{82}$$

The latter expression includes the effect of partial saturation on the effective stress field (tensile stress is positive).

For the solid phase behaviour, the isotropic solid density variation is linked to the variations of pore water pressure and mean effective stress by [DC93, Cou04]:

$$\frac{\dot{\rho}_s}{\rho_s} = \frac{(b - \Phi)\, S_{r,w}\, \dot{p}_w - \dot{\sigma}'}{(1 - \Phi)\, K_s} \tag{83}$$

The time derivative of the porosity is obtained by solid mass conservation $\dot{M}_s = 0$ and reads:

$$\dot{\Phi} = (1-\Phi)\left(\frac{\dot{\rho}_s}{\rho_s} + \frac{\dot{\Omega}}{\Omega}\right) = (1-\Phi)\left(\frac{(b-\Phi)S_{r,w}\,\dot{p}_w - \dot{\sigma}'}{(1-\Phi)\,K_s} + \frac{\dot{\Omega}}{\Omega}\right) \tag{84}$$

Furthermore, the time derivative of the water mass in Eq. 75 becomes by including the fluid compressibility, the porosity variation, and by considering a unit mixture volume:

$$\dot{M}_w = \rho_w\left(\frac{\dot{p}_w}{\chi_w}\,\Phi\,S_{r,w} + \frac{\dot{p}_w}{K_s}\,(b-\Phi)\,S_{r,w}^2 + \left(\frac{\dot{\Omega}}{\Omega} - \frac{\dot{\sigma}'}{K_s}\right)S_{r,w} + \Phi\,\dot{S}_{r,w}\right) \tag{85}$$

The above expressions can be rewritten under poroelastic assumption:

$$\dot{\sigma}' = K\,\dot{\varepsilon}_v = K\,\frac{\dot{\Omega}}{\Omega} \tag{86}$$

and using the Biot's coefficient expression of Eq. 81. The equations become:

$$\frac{\dot{\rho}_s}{\rho_s} = \frac{(b-\Phi)S_{r,w}\,\dot{p}_w - K\,\frac{\dot{\Omega}}{\Omega}}{(1-\Phi)\,K_s} \tag{87}$$

$$\dot{\Phi} = (b-\Phi)\left(\frac{S_{r,w}}{K_s}\,\dot{p}_w + \frac{\dot{\Omega}}{\Omega}\right) \tag{88}$$

$$\dot{M}_w = \rho_w\left(\frac{\dot{p}_w}{\chi_w}\,\Phi\,S_{r,w} + \frac{\dot{p}_w}{K_s}\,(b-\Phi)\,S_{r,w}^2 + b\,\frac{\dot{\Omega}}{\Omega}\,S_{r,w} + \Phi\,\dot{S}_{r,w}\right) \tag{89}$$

Biot's theory and the equations of poroelasticity are valid only for an elastic behaviour. Extending these equations to poroplasticity [Cou95] with permanent changes in fluid mass content and in porosity requires to include the plastic material behaviour, which is complex to implement and is not included in this chapter.

According to the previous assumptions, the momentum balance equation Eq. 33 and the water mass balance equation Eq.44 remain valid provided that the different variables included in these two equations are adapted to unsaturated conditions (ρ, σ_{ij}, $\dot{M}_w$ ...).

6   Modelling of a gallery excavation

The processes of underground drilling and induced shear strain localisation are investigated at large scale. [PV92] were the first to present a numerical analysis of progressive localisation around an excavated cavity in rock with a Cosserat microstructure. In

the following, a gallery excavation is considered in a clayey rock. In the rock mass, the fractured structure around the galleries develops preferentially in the horizontal or vertical direction depending on the anisotropy of both stress state and material properties [ALN+14]. As a first large-scale approach including strain localisation, an isotropic mechanical model is used with the objective of analysing if the appearance of fractures during the drilling of galleries is governed by the anisotropy of the *in situ* stress state [PLC15]. So far, the numerical modelling of gallery drilling with the second gradient model has highlighted strain localisation but was essentially limited to mechanical analyses with isotropic initial stress state [Fer09, SaHC09].

Moreover, during the operational phases of underground openings, an air ventilation is performed inside the galleries to control the air relative humidity and temperature. This ventilation induces fluid transfers and a desaturation of the rock that must be taken into account in the coupled second gradient model.

Many studies have been performed with two-dimensional isotropic mechanical models. Our purpose is to investigate if this type of model can reproduce the *in situ* observations and measurements by incorporating the fracture modelling with strain localisation. The zone that develops around the gallery is called excavation fractured zone, and it is related to the irreversible hydro-mechanical property changes.

It should be pointed out that regularisation techniques have already been used for this type of problem. They generate results that are mesh-independent but these theories do not restore the uniqueness of the solution for the gallery excavation problem [Fer09, SaHC09]. These remarks are valid for all regularisation methods.

6.1   Numerical model

A hydro-mechanical modelling of a gallery excavation is performed in two-dimensional plane strain state. The modelled gallery corresponds to the GED gallery of the Andra's URL oriented parallel to the minor horizontal principal total stress σ_h and having a radius of 2.3 m. The initial pore water pressure and anisotropic stress state are:

$$\sigma_{x,0} = \sigma_H = 1.3\,\sigma_h = 15.6\,MPa$$

$$\sigma_{y,0} = \sigma_v = 12\,MPa$$

$$\sigma_{z,0} = \sigma_h = 12\,MPa$$

$$p_{w,0} = 4.5\,MPa$$

A schematic representation of the models, the meshes, and the boundary conditions is detailed in Fig. 11. Two meshes are used: a full gallery and a quarter of a gallery. The mesh extension of the full gallery is 120 m, both horizontally and vertically, and the spatial discretisation is performed with a total of 29040 nodes and 7440 elements. Assuming symmetry along the x and y-axes, only one quarter of the gallery can be discretised. In this case, the mesh extension is 60 m, both horizontally and vertically,

and the discretisation is performed with a total of 9801 nodes and 2480 elements. For both meshes, the initial stresses and pore water pressure are imposed at the mesh external boundary (drained boundary) and the meshes have a more refined discretisation close to the gallery. To establish the symmetry, the normal displacements and the normal water flows are blocked to a value of zero along the symmetry axes, which are therefore impervious. Nonetheless, as mentioned by [ZPV01a], a special care must be brought to the kinematic boundary conditions required to establish the symmetry. Due to the existence of gradient terms in the equilibrium equations, higher order constraints have to be characterised in addition to the classical boundary condition on the normal displacements. This second kinematic condition requires that the radial displacement u_r must be symmetric on both sides of the symmetry axes. This implies that the normal derivative of u_r, with respect to the tangential (orthoradial) direction θ, has to cancel:

$$\frac{\partial u_r}{\partial \theta} = 0 \tag{90}$$

which is equivalent to:

$$x - axis: \qquad \frac{\partial u_x}{\partial y} = 0 \tag{91}$$

$$y - axis: \qquad \frac{\partial u_y}{\partial x} = 0 \tag{92}$$

Furthermore, natural boundary conditions for the double forces, $\overline{T}_i = 0$, are assumed on the different boundaries and gravity is not taken into account.

The gallery excavation can now be considered. It is modelled by decreasing during 5 days the total stresses and the pore water pressure at the gallery wall from their initial values to the atmospheric pressure of 100 kPa. After the excavation, the calculation is extended to 1000 days under constant total radial stress, to highlight possible long-term effects (Fig. 12). This stress imposition is representative of unsupported galleries.

To model the air ventilation inside the gallery, a classical flow boundary condition is assumed and imposes the suction corresponding to the relative humidity of the cavity air at the tunnel wall. Two cases are considered for the air inside the gallery (Fig. 12). In the first case, there is no ventilation inside the gallery; thus, the air is saturated with water vapour and this maximum concentration corresponds to $RH = 100$ %. According to Kelvin's law, the corresponding pore water pressure at the gallery wall is the atmospheric pressure $p_w = 100$ kPa. The pore water pressure is then maintained constant after the end of the excavation and the rock mass remains almost saturated. In the second case, air ventilation is taken into account, since ventilation is usually realised in the galleries composing underground structures. It may drain the water from the rock, desaturate it, and modify the structure, the fracturing pattern, as well as the size of the fractured zone. Air ventilation can thus be modelled in order to observe its effects on the rock material. A theoretical ventilation, with constant air relative humidity, is envisaged to obtain a first outlook of the ventilation effect on shear banding. The air which is injected in the gallery is dryer than previously and a lower relative
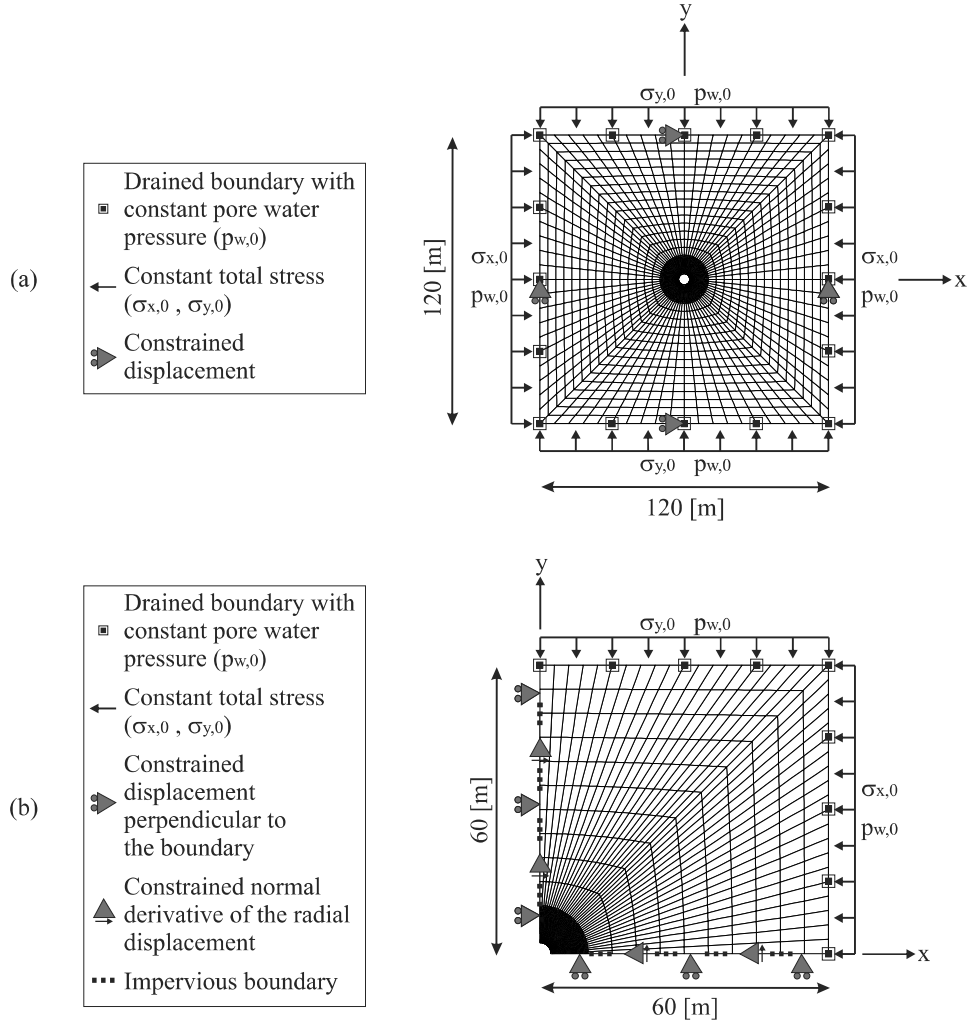
Figure 11: Schematic representation of the models used for the modelling of a gallery excavation: (a) full gallery and (b) quarter of a gallery.

humidity of 80 % with a temperature of 25 °C ($T = 298.15\ K$) are considered. Following Kelvin's law, this humidity corresponds to a pore water pressure at gallery wall of $p_w = -30.7\ MPa$. To reach this value, the decrease of p_w is performed in two steps: firstly, it decreases from its initial value to the atmospheric pressure during the excavation (5 days), and then an initiation phase of ventilation is considered (5 days) to reach the final value. After this initiation phase, a constant ventilation is maintained.

The imposed boundary conditions at gallery wall, for total stresses and pore water

pressure evolutions, are presented in Fig. 12 for the two considered cases. It is worth mentioning that the ventilation effect on the shear banding is therefore represented by the hydro-mechanical model. In fact, the ventilation influences the pore water pressures and the effective stresses, which then influence the shear strain localisation structure and behaviour.
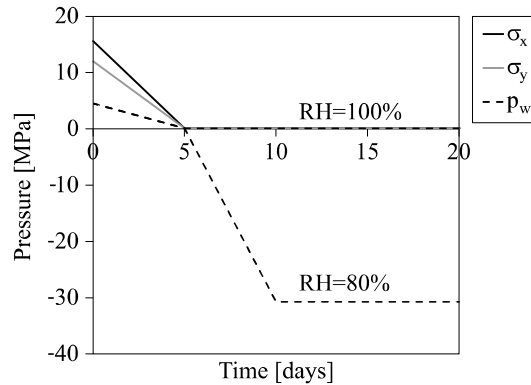

Figure 12: Imposed total stresses and pore water pressure at the gallery wall for the modelling of a gallery excavation with and without air ventilation.

The main purpose of this numerical modelling is to represent the fractures with shear strain localisation and to reproduce, as well as possible, the *in situ* measurements and observations with an isotropic mechanical model.

6.2   Influence of *in situ* stress and permeability anisotropies

Creation and evolution of the fractured zone can be observed through the evolution of shear strain localisation. The latter is not *a priori* assured to be symmetric around the gallery and many solutions could emerge [SaHC09]. To avoid any early symmetry assumption, the excavation of a full gallery is firstly modelled with incompressible solid grains $b = 1$ and no ventilation. With a circular gallery and an isotropic state, it is not possible to trigger the shear strain localisation and the deformation remains diffuse. Strain localisation can be triggered through the introduction of an imperfection in the material.

However, in case of anisotropic stress state of the rock with $\sigma_{x,0} = 15.6$ *MPa* and $\sigma_{y,0} = \sigma_{z,0} = 12$ *MPa*, the shear strain localisation appears without adding an imperfection in the rock. Fig. 13 illustrates the evolution of the strain localisation around the gallery, during and after drilling. The numerical results presented are the total deviatoric strain, the plastic zone, and the deviatoric strain increment which represents the band activity:
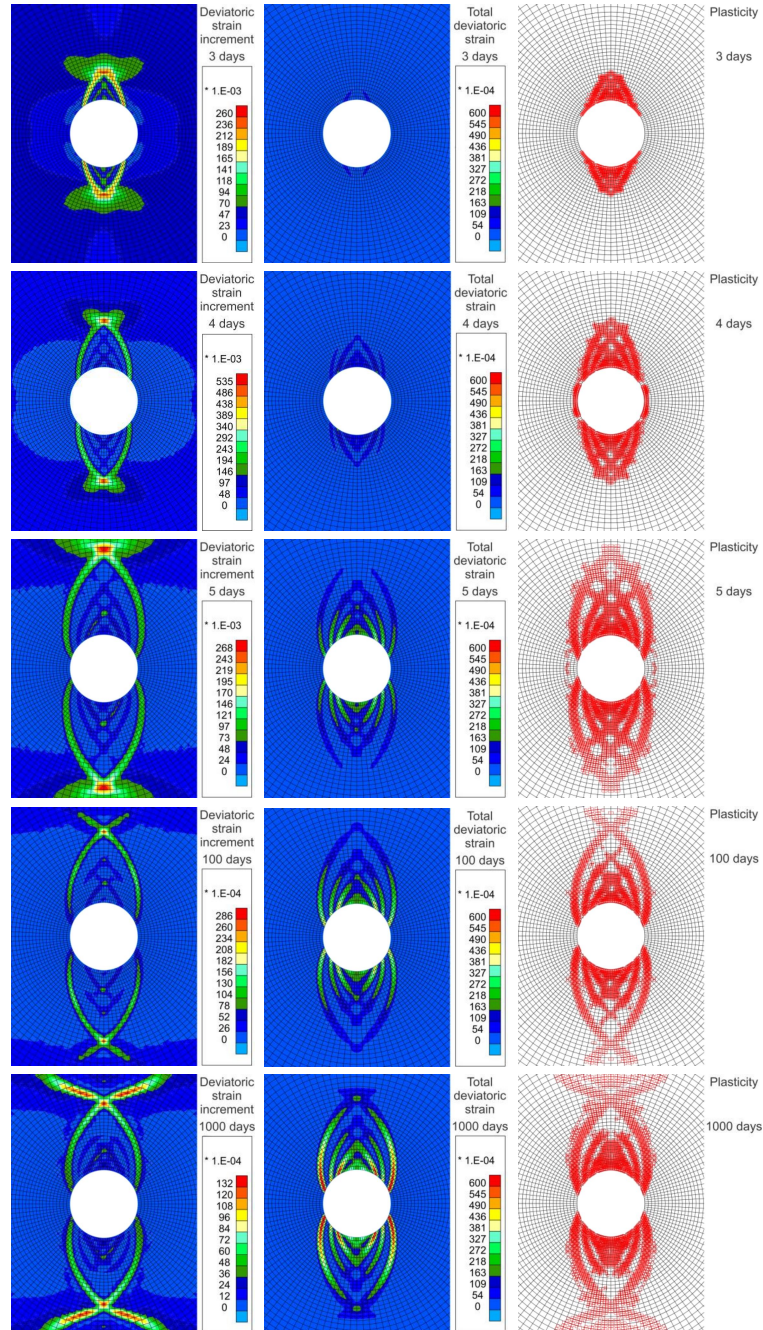
Figure 13: Evolution of strain localisation during and after the gallery excavation (5 days of excavation), for a full gallery and for a rock having anisotropic hydraulic permeability and anisotropic stress state.

$$\hat{\dot{\varepsilon}}_{eq} = \sqrt{\frac{2}{3} \, \hat{\dot{\varepsilon}}_{ij} \, \hat{\dot{\varepsilon}}_{ij}} \tag{93}$$

where $\hat{\varepsilon}_{ij}$ is the deviatoric total strain field calculated from the total strain tensor ε_{ij}:

$$\hat{\varepsilon}_{ij} = \varepsilon_{ij} - \frac{\varepsilon_{kk}}{3} \, \delta_{ij} \tag{94}$$

$$\kappa_{eq} = \frac{\hat{\dot{\varepsilon}}_{eq} \, dt}{\int \hat{\dot{\varepsilon}}_{eq} \, dt} \tag{95}$$

The modelling exhibits a symmetric chevron fracture pattern around the gallery similar to *in situ* observations for galleries parallel to σ_h. The chevron fractures appear during the excavation and are mainly concentrated above the gallery because of the material anisotropic stress state. On the contrary, introducing only the anisotropy of the intrinsic water permeability with $k_{w,h} = 4 \times 10^{-20} \, m^2$ and $k_{w,v} = 1.33 \times 10^{-20} \, m^2$ does not lead to strain localisation unless an imperfection is introduced. It means that the appearance and shape of the strain localisation are mainly due to mechanical effects linked to the anisotropic stress state. The shear banding zone develops preferentially in the direction of the minor principal stress in the gallery section.

6.3   Influence of second gradient boundary condition

The previous modelling highlights that the anisotropic stress state is at the origin of a symmetry in the localisation pattern around the gallery. Then, it would be convenient, in the following, to consider only a quarter of a gallery. However, in the context of second gradient theory, a boundary condition of higher order should be considered in addition to the classical boundary condition of constrained displacement perpendicular to the boundary [ZPV01a]. This second kinematic condition specifies that the normal derivative of the radial displacement has to cancel on the symmetry axes.

To illustrate the necessity of this second gradient boundary condition, the strain localisation pattern of Fig. 13 is compared to the pattern obtained on a quarter of a gallery. The modelling on a quarter of a gallery is computed with the specific second gradient boundary condition, and with $b = 1$ and no ventilation as previously. In Fig. 14, one can observe that using the second gradient boundary condition produces a shear strain localisation pattern that is similar to the full-gallery results. Thus, it is confirmed that, for calculation simplicity and symmetry reasons, a quarter of a gallery can be adopted for future modelling, provided that the specific second gradient boundary condition is used.

6.4   Influence of Biot's coefficient

Even if strain localisation seems to be mainly controlled by mechanical effects, hydraulic conditions can also impact the shear banding pattern. Here, the focus is on the

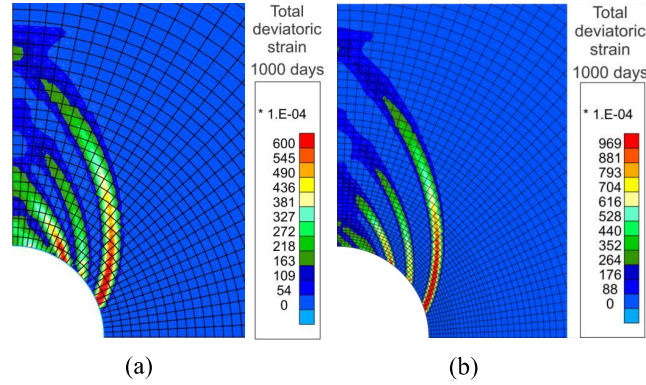(a)   (b)

Figure 14: Comparison of the strain localisation pattern at the end of the calculation for the modelling of: (a) a full gallery and (b) a quarter of a gallery with the second gradient boundary condition.

influence of Biot's coefficient for the case without ventilation. In the first calculation, it is assumed that the solid grains are incompressible, which implies $b = 1$ (Fig. 15). In the second calculation, a value of $b = 0.6$ is used (Fig. 16). Comparison of Figs. 15 and 16 indicates that the Biot's coefficient significantly influences the shear band pattern. With a value of 0.6, less bands appear and the shear strain localisation is delayed. In fact, the strain remains diffuse until the fourth day of the excavation; nonetheless, the localisation appears before the end of the excavation. This can be explained by examining the stresses close to the gallery. At the gallery wall, the total stresses and the pore water pressure are imposed. Consequently, following the Biot's effective stress definition for unsaturated materials of Eq. 82, the lower the Biot's coefficient, the higher the effective compressive stress at the gallery wall. This implies that the rock close to the gallery wall is more resistant and that the shear strain localisation appears later.

6.5   Influence of gallery ventilation

The modelling presented hereafter includes the initial anisotropies, a Biot's coefficient value of 0.6, and the gallery ventilation. The drilling phase is not influenced by the ventilation, and the same results as in Fig. 16 are obtained until 5 days of computation. The results obtained after the excavation, displayed in Fig. 17, indicate that the suction imposed at the wall strongly influences the results. Following the effective stress definition, the higher the suction, the higher the effective stress (Fig. 20). As noted before, this involves that the material is more resistant, and in this case, becomes elastic again close to the gallery. This inhibits the shear strain localisation around the gallery.
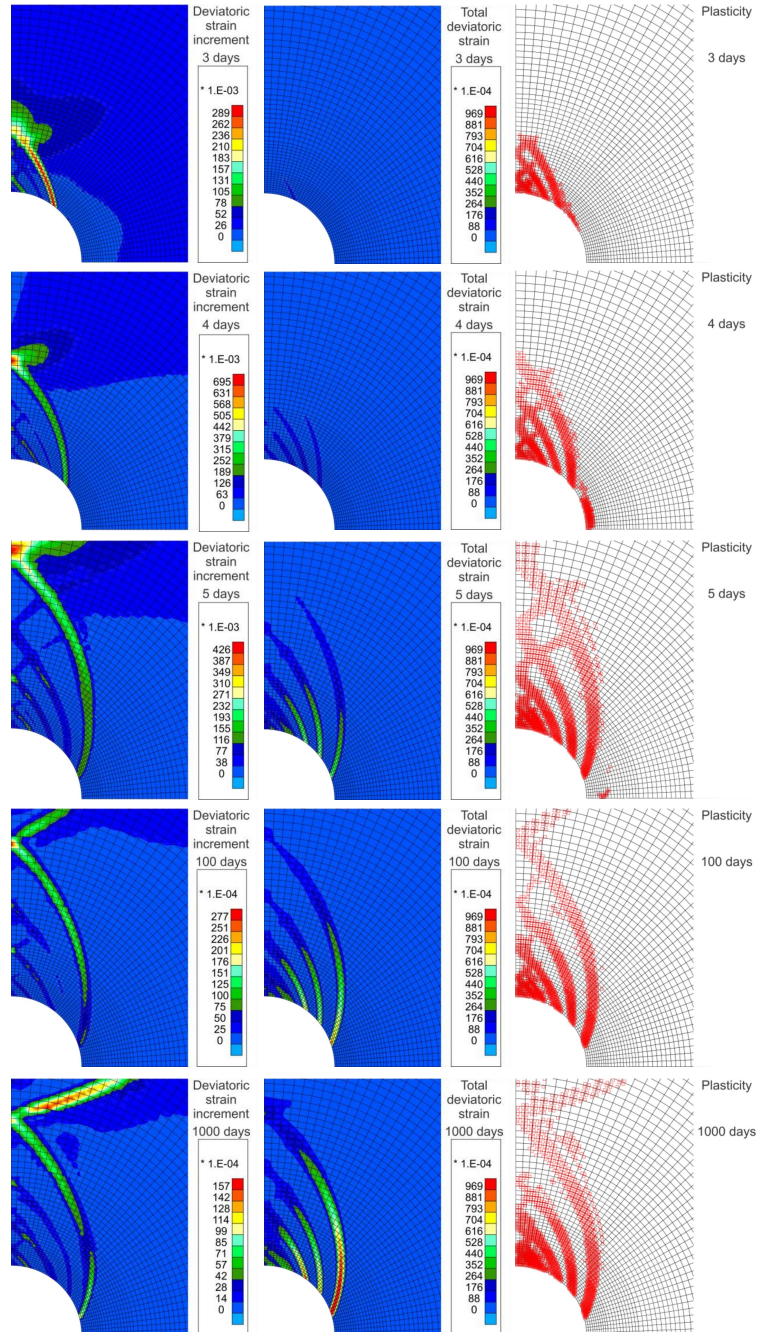
Figure 15: Evolution of strain localisation during and after gallery excavation (5 days of excavation), without gallery ventilation and for a Biot's coefficient value of 1.
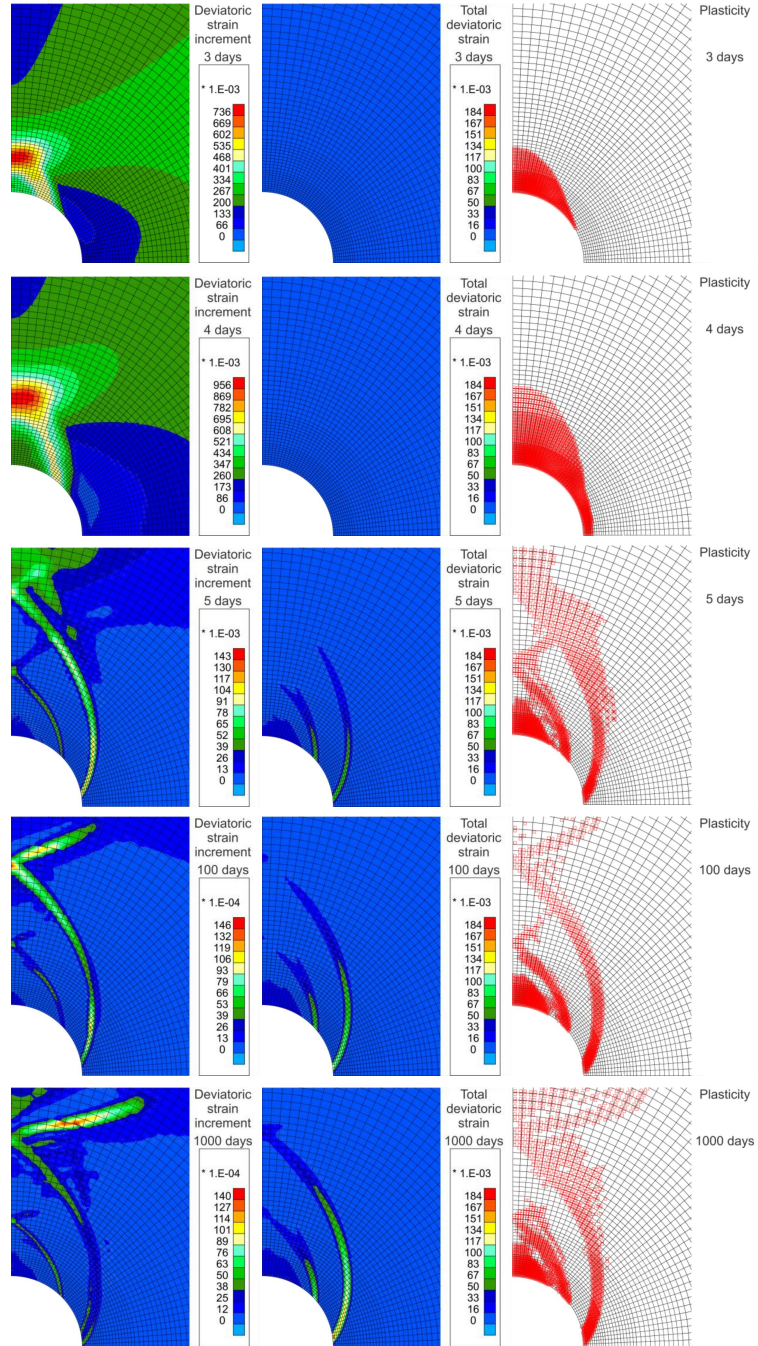
Figure 16: Evolution of strain localisation during and after gallery excavation (5 days of excavation), without gallery ventilation and for a Biot's coefficient value of 0.6.
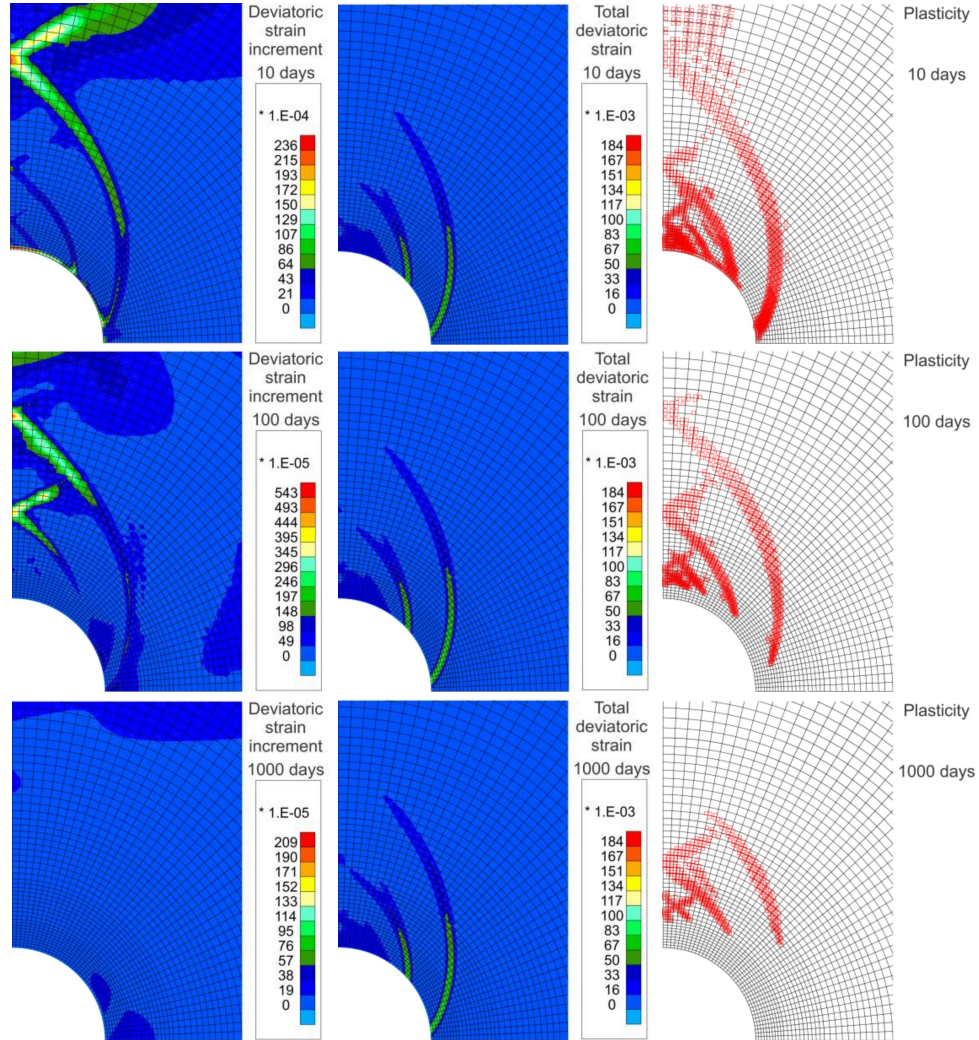
Figure 17: Evolution of strain localisation after gallery excavation, with gallery ventilation and for a Biot's coefficient value of 0.6.

Various numerical results, coming from the gallery wall and the rock mass, are interpreted hereafter in order to emphasize the influence of the gallery air ventilation. The results come from the selected cross-sections and observation points on gallery wall that are presented in Fig. 18. The vertical cross-section goes through the shear bands and the results along it highlights the effects of strain localisation, which is not the case for the horizontal cross-section. Furthermore, the results are compared for the cases considering ($RH = 80$ %) or not ($RH = 100$ %) the ventilation.
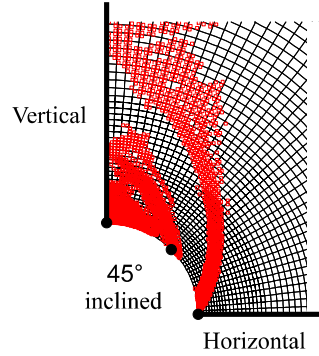
Figure 18: Positions of cross-sections and gallery wall observation points.

The evolution of pore water pressure for the vertical and horizontal cross-sections is detailed in Fig. 19. In the rock mass, an increase of pressure is observed in the vertical direction and a decrease in the horizontal direction up to a radial distance of about 30 m. These overpressures are related to the hydro-mechanical coupling induced by the anisotropy of the initial stress state. The influence of the strain localisation bands is visible vertically but not horizontally. It is illustrated by the fluctuations of the pore water pressure in limited zones, with a decrease in the shear band. The influence of the shear band can be mostly observed during the first 50 days of calculation then it tends to vanish. This is due to the strain increment inside the bands (band activity) and the hydro-mechanical coupling. As expected, the influence of the ventilation is marked close to the gallery wall, but tends to disappear deeper in the rock.

The stress paths at the gallery wall are detailed in Fig. 20 where q is the deviatoric stress:

$$q = \sqrt{3}\, II_{\hat{\sigma}'} \tag{96}$$

and p' is the mean effective stress. As mentioned before, in the case of ventilation, the effective stresses are much higher due to suction. This explains the difference between the stress paths of the modelling with and without ventilation, after the end of the drilling phase.

All these results are evidences that noticeable differences exist whether ventilation is applied or not. For the modelling with ventilation, p_w remains negative close to the gallery (Fig. 19), the effective stresses increase after the excavation (Fig. 20) and the material becomes elastic again. Consequently, the desaturation of the rock close to the gallery inhibits the shear strain localisation (Fig. 17), which has the effect of restricting further deformation. On the contrary, without ventilation, p_w close to the gallery wall increases after the excavation (Fig. 19), the effective stresses reduce (Fig. 20) and the material remains partly plastic close to the gallery (Fig. 16). This increases the deformation and the gallery convergence.

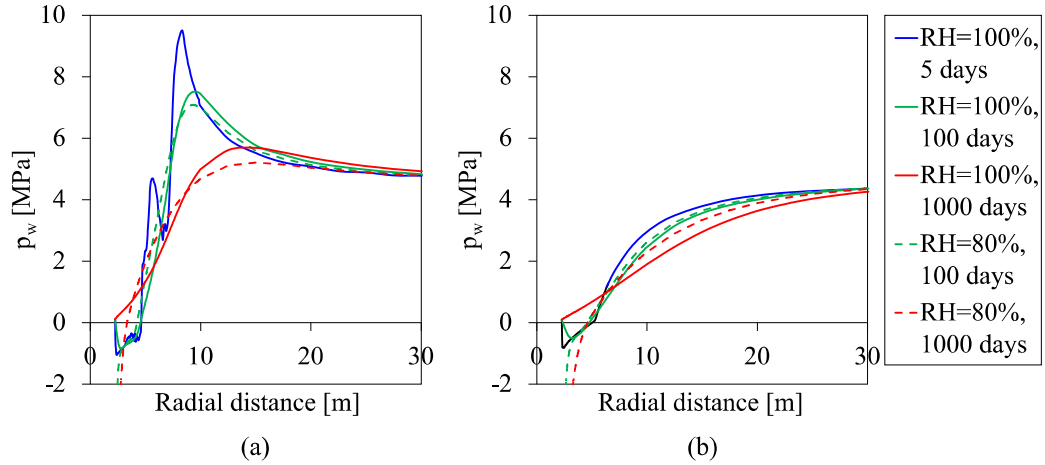If the problem is studied with an isotropic model, without considering strain locali-

Figure 19: Evolution of pore water pressure along (a) vertical and (b) horizontal cross-sections, after gallery excavation.
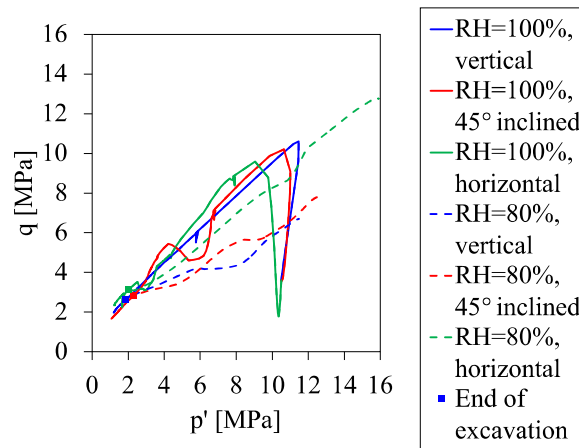

Figure 20: Stress paths at the gallery wall, during and after gallery excavation.

sation but modelling the gallery ventilation, then the horizontal and vertical convergences are more or less equal. Only the fracturing and strain localisation processes permit to produce the convergence anisotropy. In fact, neither the fracturing pattern nor the gallery convergence can be well reproduced with classical approach [PC16]. The creation of fractures, globally above the gallery due to the material anisotropic stress state, increases both the vertical and the horizontal convergences. In that latter direction, the proximity of the shear bands induces excessive deformations. In the

long term, the delayed deformations that are observed in saturated conditions are explained by consolidation. In contrast to this, when gallery ventilation is reproduced, the material close to the gallery wall becomes elastic again which restricts the plastic deformation and convergence in the long term. The performed numerical modelling highlights the effect of gallery ventilation on the hydraulic transfer and progressive drainage of the surrounding rock. However, the considered air ventilation is theoretical and a real ventilation could be considered [CCP$^+$13], [PTC16]. Moreover, the water transfer and its kinetics close to the gallery are mainly conditioned by the hydro-mechanical property changes inside the excavation damaged zone. In fact, the damaged zone developing around galleries due to the drilling processis composed of fractures having a significant irreversible impact on flow and transport characteristics [TBD05]. For a shear banding approach, the impact of fracturing on the transport properties can be addressed by associating the intrinsic permeability increase with mechanical deformation [PTC16], which is amplified in the strain localisation discontinuities. Such dependence permits to reproduce a significant permeability increase of several orders of magnitude in the excavation damaged zone [PTC16], in agreement with available experimental measurements [ALN$^+$14].

7   Conclusions

Rupture in geomaterials is often preceded by a localization of the deformations within thin bands. The strain localization is thus an important process, which has been studied both experimentally and theoretically. The developments of geomechanics in the field of coupled multiphysic processes impose the study of strain localization to these new conditions. Interactions between the different processes can indeed occur. Furthermore, the numerical modelling of shear bands with classical finite element suffers of a mesh dependency problem. An internal length scale has to be introduced in the model. Among the different regularization techniques, we propose a second gradient coupled model for an application to gallery excavation. It has been shown that the model regularizes the solution but does not restore its uniqueness. The extension of such theories to other multiphysic context is more an experimental problem than a numerical one. Experiments still have to exhibit the influence of temperature, suction or chemical concentration on the occurrence and the thickness of the strain localization!

References

[ABS03]   K Alshibli, S Batiste, and S Sture. Strain Localization in Sand: Plane Strain versus Triaxial Compression. *J Geotech Geoenviron Eng*, 129(6):483–494, 2003.

[Aif84]   E C Aifantis. On the microstructural origin of certain inelastic models. *J Eng Mater Technol*, 106(4):326–330, 1984.

[ALN$^+$14]   G Armand, F Leveau, C Nussbaum, R de La Vaissiere, A Noiret, D Jaeggi, P Landrein, and C Righini. Geometry and properties of the excavation-induced fractures at the Meuse/Haute-Marne URL drifts. *Rock Mech Rock Eng*, 47(1):21–41, 2014.

[BA95]   R I Borja and E Alarcon. A mathematical framework for finite strain elastoplastic consolidation part 1: Balance laws, variational formulation, and linearization. *Comput Methods Appl Mech Engrg*, 122(1-2):145–171, 1995.

[BBC84]   Z P Bazant, T B Belytschko, and T P Chang. Continuum Theory for Strain Softening. *J Eng Mech*, 110(12):1666–1692, 1984.

[BCC06]   P Bésuelle, R Chambon, and F Collin. Switching deformation modes in post-localization solutions with a quasibrittle material. *J Mech Mater Struct*, 1(7):1115–1134, 2006.

[BDR00]   P Bésuelle, J Desrues, and S Raynaud. Experimental characterisation of the localisation phenomenon inside a vosges sandstone in a triaxial cell. *Int J Rock Mech Min Sci*, 37(8):1223–1237, 2000.

[Bio41]   M A Biot. General theory for three-dimensional consolidation. *J Appl Phys*, 12(2):155–164, 1941.

[BW57]   M A Biot and D G Willis. The Elastic Coefficients of the Theory of Consolidation. *J Appl Mech*, 24:594–601, 1957.

[CC09]   E Cosserat and F Cosserat. *Théorie des Corps Déformables*. Hermann, Paris, 1909.

[CCC01]   R Chambon, S Crochepeyre, and R Charlier. An algorithm and a method to search bifurcation points in non-linear problems. *Int J Numer Meth Engng*, 51(3):315–332, 2001.

[CCC06]   F Collin, R Chambon, and R Charlier. A finite element method for poro mechanical modelling of geotechnical problems using local second gradient models. *Int J Numer Meth Engng*, 65(11):1749–1772, 2006.

[CCC09]   F Collin, D Caillerie, and R Chambon. Analytical solutions for the thick-walled cylinder problem modeled with an isotropic elastic second gradient constitutive equation. *Int J Solids Struct*, 46(22-23):3927–3937, 2009.

[CCH98]   R Chambon, D Caillerie, and N El Hassan. One-dimensional localisation studied with a second grade model. *Eur J Mech A-Solid*, 17(4):637–656, 1998.

[CCM01]   R Chambon, D Caillerie, and T Matsushima. Plastic continuum with microstructure, local second gradient theories for geomaterials : localization studies. *Int J Solids Struct*, 38(46-47):8503–8527, 2001.

[CCP+13] R Charlier, F Collin, B Pardoen, J Talandier, J P Radu, and P Gerard. An unsaturated hydro-mechanical modelling of two in-situ experiments in Callovo-Oxfordian argillite. *Eng Geol*, 165:46–63, 2013.

[CLC09] F Collin, S Levasseur, and R Chambon. Numerical post failure methods in multiphysical problems. *Eur J Environ Civ Eng*, 13(7-8):983–1004, 2009.

[CM04] R Chambon and J C Moullet. Uniqueness studies in boundary value problems involving some second gradient models. *Comput Methods Appl Mech Engrg*, 193(27-29):2771–2796, 2004.

[Cou73] C A Coulomb. Essai sur une application des règles de maximis et minimis à quelques problèmes de statique, relatifs à l'architecture. *Académie Royale des Sciences*, 7:343–382, 1773.

[Cou95] O Coussy. *Mechanics of Porous Continua*. John Wiley & Sons, Chichester, 1995.

[Cou04] O Coussy. *Poromechanics*. John Wiley & Sons, Chichester, 2004.

[CRB97] R Charlier, J P Radu, and J D Barnichon. Water movement effect on the strain localisation during a biaxial compression. In G Pande and S Pietruszczak, editors, *Numerical Models in Geomechanics, NUMOG VI*, pages 219–224, Rotterdam, 1997. Balkema.

[dBM92] R de Borst and H B Mühlhaus. Gradient-dependent plasticity: Formulation and algorithm aspects. *Int J Numer Meth Engng*, 35(3):521–539, 1992.

[DC93] E Detournay and A H D Cheng. *Comprehensive Rock Engineering: Principles, Practice and Projects*, volume 2 Analysis and Design Method, chapter 5 Fundamentals of Poroelasticity, pages 113–171. Pergamon Press, Oxford, 1993.

[Des84] J Desrues. *La localisation de la déformation dans les matériaux granulaires*. PhD thesis, Université Joseph Fourier, Institut National Polytechnique, Grenoble, 1984.

[Des05] J Desrues. Hydro-mechanical coupling and strain localization in saturated porous media. *Rev Eur Génie Civ*, 9(5-6):619–634, 2005.

[Die03] M S Diederichs. Rock Fracture and Collapse Under Low Confinement Conditions. *Rock Mech Rock Eng*, 36(5):339–381, 2003.

[DV04] J Desrues and G Viggiani. Strain localization in sand: an overview of the experimental results obtained in Grenoble using stereophotogrammetry. *Int J Numer Anal Meth Geomech*, 28(4):279–321, 2004.

[EV98]   W Ehlers and W Volk. On theoretical and numerical methods in the theory of porous media based on polar and non-polar elasto-plastic solid materials. *Int J Solids Struct*, 35(34-35):4597–4617, 1998.

[Fer09]   R Fernandes. *Modélisation numérique objective des problèmes hydromécaniques couplés dans le cas des géomatériaux*. PhD thesis, Université Joseph Fourier, Grenoble, 2009.

[FHMV96]   R Finno, W Harris, M Mooney, and G Viggiani. Strain localization and undrained steady state of sands. *J Geotech Engrg*, 122(6):462–473, 1996.

[FHMV97]   R Finno, W Harris, M Mooney, and G Viggiani. Shear bands in plane strain compression of loose sand. *Géotechnique*, 47(1):149–165, 1997.

[Ger73]   P Germain. The method of virtual power in continuum mechanics. Part 2 Microstructure. *SIAM J Appl Math*, 25(3):556–575, 1973.

[GSH12]   N Guy, D M Seyedi, and F Hild. A probabilistic nonlocal model for crack initiation and propagation in heterogeneous brittle materials. *Int J Numer Meth Engng*, 90(8):1053–1072, 2012.

[HD93]   C Han and A Drescher. Shear bands in biaxial tests on dry coarse sand. *Soils Found*, 33(1):118–132, 1993.

[JKC14]   Gwendal Jouan, Panagiotis Kotronis, and Frédéric Collin. Using a second gradient model to simulate the behaviour of concrete structural elements. *Finite Elements in Analysis and Design*, 90:50 – 60, 2014.

[JS88]   Y S Jenq and S P Shah. Mixed-mode fracture of concrete. *Int J Fracture*, 38(2):123–142, 1988.

[KCB+07]   P Kotronis, F Collin, P Bésuelle, R Chambon, and J Mazars. Local Second Gradient Models and Damage Mechanics: 1D Post-Localization Studies in Concrete Specimens. In G Exadaktylos and I Vardoulakis, editors, *Bifurcation, Instabilities and Degradation in Geomechanics*, pages 127–142. Springer, 2007.

[KGDL06]   H D V Khoa, I O Georgopoulos, F Darve, and F Laouafa. Diffuse failure in geomaterials: Experiments and modelling. *Comput Geotech*, 33(1):1–14, 2006.

[LB88]   D Lasry and T Belytschko. Localization limiters in transient problems. *Int J Solids Struct*, 24(6):581–597, 1988.

[LBD+07]   N Lenoir, M Bornert, J Desrues, P Bésuelle, and G Viggiani. Volumetric digital image correlation applied to X-ray microtomography images from triaxial compression tests on argillaceous rock. *Strain*, 43(3):193–205, 2007.

[MCC02]   T Matsushima, R Chambon, and D Caillerie. Large strain finite element analysis of a local second gradient model: application to localization. *Int J Numer Meth Engng*, 54(4):499–521, 2002.

[MD99]   M Mokni and J Desrues. Strain localisation measurements in undrained plane-strain biaxial test on Hostun RF sand. *Mech Cohes-Frict Mat*, 4(4):419–441, 1999.

[Min64]   R D Mindlin. Micro-structure in linear elasticity. *Arch Ration Mech An*, 16(1):51–78, 1964.

[Min65]   R D Mindlin. Second gradient of strain and surface-tension in linear elasticity. *Int J Solids Struct*, 1:417–438, 1965.

[MSC14]   F Marinelli, Y Sieffert, and R Chambon. Hydromechanical modelling of an initial boundary value problem: Studies of non-uniqueness with a second gradient continuum. *Int J Solids Struct*, 2014.

[Mua76]   Y Mualem. A new model for predicting the hydraulic conductivity of unsaturated porous media. *Water Resour Res*, 12(3):513–522, 1976.

[NL08]   M Nuth and L Laloui. Effective stress concept in unsaturated soils: Clarification and validation of a unified framework. *Int J Numer Anal Meth Geomech*, 32(7):771–801, 2008.

[PC16]   B Pardoen and F Collin. Modelling the influence of strain localisation and viscosity on the behaviour of underground drifts drilled in claystone. *Comput Geotech*, 2016. in press.

[PCB87]   G Pijaudier-Cabot and Z P Bazant. Nonlocal damage theory. *J Eng Mech*, 113(10):1512–1533, 1987.

[PdBB⁺96]   R H J Peerlings, R de Borst, W A M Brekelmans, J H P de Vree, and I Spee. Some observations on localisation in non-local and gradient damage models. *Eur J Mech A/Solids*, 15(6):937–953, 1996.

[PdBBdV96]   R H J Peerlings, R de Borst, W A M Brekelmans, and J H P de Vree. Gradient enhanced damage for quasi-brittle materials. *Int J Numer Meth Engng*, 39(19):3391–3403, 1996.

[PGdBB01]   R H J Peerlings, M G D Geers, R de Borst, and W A M Brekelmans. A critical comparison of nonlocal and gradient-enhanced softening continua. *Int J Solids Struct*, 38(44-45):7723–7746, 2001.

[PLC15]   B Pardoen, S Levasseur, and F Collin. Using Local Second Gradient Model and Shear Strain Localisation to Model the Excavation Damaged Zone in Unsaturated Claystone. *Rock Mech Rock Eng*, 48(2):691–714, 2015. doi: 10.1007/s00603-014-0580-2.

[PM81]   S T Pietruszczak and Z Mróz. Finite element analysis of deformation of strain-softening materials. *Int J Numer Meth Engng*, 17(3):327–334, 1981.

[PTC16]   B Pardoen, J Talandier, and F Collin. Permeability evolution and water transfer in the excavation damaged zone of a ventilated gallery. *Int J Rock Mech Min Sci*, 85:192–208, 2016. 10.1016/j.ijrmms.2016.03.007.

[PV92]   P C Papanastasiou and I G Vardoulakis. Numerical treatment of progressive localization in relation to borehole stability. *Int J Numer Anal Meth Geomech*, 16(6):389–424, 1992.

[Ric76]   J R Rice. The localization of plastic deformation. In W T Koiter, editor, *Theoretical and Applied Mechanics*, volume 1, pages 207–220. North-Holland Publishing Company, 1976.

[RR75]   J W Rudnicki and J R Rice. Conditions for the localisation of deformation in pressure sensitive dilatant materials. *J Mech Phys Solids*, 23:371–394, 1975.

[SaHC09]   Y Sieffert, S al Holo, and R Chambon. Loss of uniqueness of numerical solutions of the borehole problem modelled with enhanced media. *Int J Solids Struct*, 46(17):3173–3197, 2009.

[Ske60]   A W Skempton. Effective stress in soils, concrete and rocks. In *Pore Pressure and Suction in Soils*, pages 4–16, London, 1960. Butterworths.

[TBD05]   C F Tsang, F Bernier, and C Davies. Geohydromechanical processes in the Excavation Damaged Zone in crystalline rock, rock salt, and indurated and plastic clays - in the context of radioactive waste disposal. *Int J Rock Mech Min Sci*, 42(1):109–125, 2005.

[Tou62]   R Toupin. Elastic materials with couple-stresses. *Arch Ration Mech An*, 11(1):385–414, 1962.

[vG80]   M T van Genuchten. A closed-form equation for predicting the hydraulic conductivity of unsaturated soils. *Soil Sci Soc Am J*, 44(5):892–898, 1980.

[VGG78]   I Vardoulakis, M Goldscheider, and Q Gudehus. Formation of shear bands in sand bodies as a bifurcation problem. *Int J Numer Anal Meth Geomech*, 2(2):99–128, 1978.

[VS95]   I Vardoulakis and J Sulem. *Bifurcation Analysis in Geomechanics*. Blackie Academic and Professional, 1995.

[WW10]   S Wu and X Wang. Mesh Dependence and Nonlocal Regularization of One-Dimensional Strain Softening Plasticity. *J Eng Mech*, 136(11):1354–1365, 2010.

[Zau89]   E Zauderer. *Partial Differential Equations of Applied Mathematics.* Wiley, Chichester,UK, second ed. edition, 1989.

[ZPV01a]   A Zervos, P Papanastasiou, and I Vardoulakis. Modelling of localisation and scale effect in thick-walled cylinders with gradient elastoplasticity. *Int J Solids Struct*, 38(30-31):5081–5095, 2001.

[ZPV01b]   A Zervos, P Papanastasious, and I Vardoulakis. A finite element displacement formulation for gradient elastoplasticity. *Int J Numer Meth Engng*, 50(6):1369–1388, 2001.

[ZSS01]   H W Zhang, L Sanavia, and B A Schrefler. Numerical analysis of dynamic strain localisation in initially water saturated dense sand with a modified generalised plasticity model. *Comput Struct*, 79(4):441–459, 2001.

[ZT00]   O C Zienkiewicz and R L Taylor. *The Finite Element Method.* Butterworth-Heinemann, Stonchem, MA, fifth edition edition, 2000.